Manuscript accepted for publication in Agricultural and Forest Meteorology.

DOI: 10.1016/j.agrformet.2023.109408.

Link to the published paper: https://doi.org/10.1016/j.agrformet.2023.109408

STEEP: a remotely-sensed energy balance model for evapotranspiration estimation in seasonally dry tropical forests

Ulisses A. Bezerra[a*], John Cunha[a], Fernanda Valente[b], Rodolfo L. B. Nóbrega[c,d], João M. Andrade[e], Magna S. B. Moura[f], Anne Verhoef[g], Aldrin M. Perez-Marin[h], Carlos O. Galvão[a]

[a]Federal University of Campina Grande, Centre for Natural Resources and Technology, Campina Grande, Brazil

[b]Forest Research Centre (CEF), School of Agriculture, University of Lisbon, Tapada da Ajuda, 1349-017 Lisbon, Portugal

[c]University of Bristol, School of Geographical Sciences, University Rd, Bristol, BS8 1SS, UK

[d]Imperial College London, Georgina Mace Centre for the Living Planet, Department of Life Sciences, Silwood Park Campus, Buckhurst Road, Ascot, SL5 7PY, UK

[e]Federal University of Pernambuco, Department of Civil and Environmental Engineering, Recife, Brazil

[f]Empresa Brasileira de Pesquisa Agropecuária, Embrapa Semiárido, Petrolina, Brazil

[g]The University of Reading, Department of Geography and Environmental Science, UK

[h]Instituto Nacional do Semiárido/Núcleo de Desertificação e Agroecologia, Campina Grande, Brazil

*Corresponding author: ulisses.alencar@estudante.ufcg.edu.br; ulisses.alencar17@gmail.com

Highlights

- STEEP is a RS-based SEB model from a one-source bulk transfer equation for SDTF.
- STEEP includes improved representations of phenology and soil moisture for SDTF.
- STEEP is tested against eddy covariance data from the largest SDTF in South America.
- STEEP exhibits satisfactory metrics and outperforms SEBAL, MOD16, and PMLv2.

Abstract

Improvement of evapotranspiration (ET) estimates using remote sensing (RS) products based on multispectral and thermal sensors has been a breakthrough in hydrological research. In large-scale applications, methods that use the approach of RS-based surface energy balance (SEB) models often rely on oversimplifications. The use of these models for Seasonally Dry Tropical Forests (SDTF) has been challenging due to incompatibilities between the assumptions underlying those models and the specificities of this environment, such as the highly contrasting phenological phases or ET being mainly controlled by soil–water availability. We developed a RS-based SEB model from

a one-source bulk transfer equation, called Seasonal Tropical Ecosystem Energy Partitioning (STEEP). Our model uses the plant area index to represent the woody structure of the plants in calculating the moment roughness length. We included the parameter kB^{-1} and its correction using RS soil moisture in the calculation of the aerodynamic resistance for heat transfer. Besides, λET caused by remaining water availability in endmembers pixels was quantified using the Priestley-Taylor equation. We implemented the algorithm on Google Earth Engine, using freely available data. To evaluate our model, we used eddy covariance data from four sites in the Caatinga, the largest SDTF in South America, in the Brazilian semiarid region. Our results show that STEEP increased the accuracy of ET estimates without requiring any additional climatological information. This improvement is more pronounced during the dry season, which, in general, ET for these SDTF is overestimated by traditional SEB models, such as the Surface Energy Balance Algorithms for Land (SEBAL). The STEEP model had similar or superior behavior and performance statistics relative to global ET products (MOD16 and PMLv2). This work contributes to an improved understanding of the drivers and modulators of the energy and water balances at local and regional scales in SDTF.

Keywords: Sensible heat flux, Aerodynamic resistance for heat transfer, Surface energy balance, Caatinga, Google Earth Engine

1. Introduction

Quantifying evapotranspiration (ET) is one of the largest research challenges in hydrology because ET is driven by a complex combination of atmospheric, vegetation, edaphic, and terrain characteristics (Wang et al., 2016; Bhattarai et al., 2017). The traditional techniques to quantify ET, e.g. Bowen ratio or eddy covariance system (EC), are limited to areas up to ~10 km² (Allen et al., 2011; Anapalli et al., 2016; Mcshane et al., 2017; Mallick et al., 2018; Chu et al., 2021). Over the past decades, models based on satellite remote sensing (RS) data have been increasingly developed and applied to estimate ET for multiple temporal and spatial scales (Anderson et al., 2011; Chen and Liu, 2020). RS-based surface energy balance (SEB) models estimate ET in terms of energy per unit area (e.g. W/m²), i.e. by latent heat flux, λET, where λ is the latent heat of vaporization of water (Shuttleworth, 2012; Barraza et al., 2017; Trebs et al., 2021). SEB models obtain λET by subtracting the soil heat (G) and sensible heat (H) fluxes from the net radiation (R_n). Estimates of R_n

obtained with RS data have been improving, and this flux can nowadays be estimated with acceptable precision (Allen et al., 2011; Ferreira et al., 2020). The $G{:}R_n$ ratio can be predicted with reasonable accuracy through the use of empirical relationships with soil, vegetation, and temperature characteristics (Bastiaanssen, 1995; Murray and Verhoef, 2007; Allen et al., 2011; Danelichen et al., 2014). Challenges in estimating *λET* as a residual of the energy balance are mostly associated with the uncertainties in *H* (Gokmen et al., 2012; Paul et al., 2014; Mohan et al., 2020a, Mohan et al., 2020b; Costa-Filho et al., 2021). The bulk heat transfer calculation that is used to compute *H* involves variables related to the temperature gradient and to the aerodynamic resistance for heat transfer (*rah*). If any of these variables are poorly estimated, the performance of SEB models will be reduced (Verhoef et al., 1997a, b; Su et al., 2001; Gokmen et al., 2012; Costa-Filho et al., 2021; Liu et al., 2021; Trebs et al., 2021).

The difference between the aerodynamic surface temperature and air temperature (*dT*) drives *H*. However, the lack of techniques to measure the aerodynamic surface temperature required strategies to use the radiometric land surface temperature (LST) as an alternative. Bastiaanssen et al. (1998), when creating the Surface Energy Balance Algorithms for Land (SEBAL), proposed that *dT* can be estimated with a linear relationship on LST. This requires identifying areas with contrasting extreme conditions in terms of cover and humidity, e.g., dry bare and well-watered soil surfaces, commonly known as hot/dry and cold/wet endmembers, respectively. The sensible heat transfer equation in conjunction with the surface energy balance in hot/dry and cold/wet endmembers allows one to obtain the coefficients of the linear relationship between *dT* and LST. Bastiaanssen et al. (1998) proposed the selection of endmembers by assuming that *H* in the cold/wet endmember and *λET* in the hot/dry endmember are zero. However, these assumptions are not necessarily valid (Singh and Irmak, 2011; Singh et al., 2012). The cold/wet endmember refers to an area with a well-irrigated crop surface having ground fully covered by vegetation, so it can be assumed that a non-negligible amount of sensible heat can still be generated by such a surface. Similarly, for the hot/dry endmember, an area dominated by bare soil, there may be a *λET* resulting from antecedent rainfall events, hereafter referred to as remaining *λET*. Some studies have quantified *H* and *λET* in hot/dry and cold/wet endmembers (Trezza, 2006; Allen et al., 2007; Singh and Irmak, 2011); they have shown that this quantification produces a better approximation of daily ET.

Based on the Monin-Obukhov similarity theory, *rah* is defined as a function of the momentum (*z0m*) and heat (*z0h*) roughness lengths. Theoretically, the sum of the zero plane displacement height (*d0*) together with *z0h* defines the level of the effective source of sensible heat (Thom, 1972; Chehbouni et al., 1996; Gokmen et al., 2012) and, therefore, *z0h* constitutes one of the most crucial parameters for the accurate calculation of *H* (Verhoef et al., 1997a; Su et al., 2001). However, as *z0h* cannot be measured directly, it is commonly calculated via the dimensionless parameter kB^{-1} formulated to express the excess resistance of heat transfer compared to momentum transfer (Owen and Thomson, 1963). In RS-based SEB models, oversimplifications are present in the calculation of *rah*, e.g. different land use types are represented by the same values for *z0h* (Bastiaanssen et al., 2005; Allen et al., 2007) and kB^{-1} (Bastiaanssen et al., 1998), or the values for the aerodynamic parameters are kept constant in time and space. However, these parameters should not be considered constant, nor set to zero, because this can lead to large inaccuracies in the estimates of *H* (Verhoef et al., 1997a) and, consequently, of λET (Liu et al., 2007; Paul et al., 2014; Liu et al., 2021). Studies have shown that kB^{-1} typically ranges from 1 to 12, depending on the dominant surface coverage (Kustas et al., 1989a; Troufleau et al., 1997; Verhoef et al., 1997a; Lhomme et al., 2000; Su et al., 2001). Studies confirm that if appropriate values of kB^{-1} are used, *H* can be accurately estimated using LST via the bulk transfer method (Stewart et al., 1994; Su et al., 2001; Jia et al., 2003; Paul et al., 2013).

Another problem with RS-based SEB models is that these methods are imprecise when applied to non-agricultural environments, such as forests, deserts, sparse savannahs or rangelands, and riparian systems, because of the heterogeneous nature of the vegetation, terrain, soils, and water availability in these environments. This causes the flux estimates obtained with the SEB methods, and the underlying aerodynamic parameters, to be highly variable (Allen et al., 2011; Gokmen et al., 2012; Barraza et al., 2017; Chen and Liu, 2020; Costa-Filho et al., 2021). This is especially true in Seasonally Dry Tropical Forests (SDTF) regions, where there is a large spatio-temporal variation in vegetation density, in vegetation structural parameters such as canopy height, crown shape and branching, and water availability. SDTF are an important tropical biome and one of the most threatened ecoregions of the world (Moro et al., 2015; Pennington et al., 2018). SDTF are broadly defined as forest formations in tropical regions characterised by marked seasonality in

rainfall distribution, resulting in a prolonged dry season that usually lasts five or six months (Pennington et al., 2009; Paloschi et al., 2020). The most extensive contiguous areas of SDTF are in the neotropics, comprising more than 60% of the remaining global stands of this vegetation (Miles et al., 2006; Queiroz et al., 2017). The physiognomies exhibited by SDTF are heterogeneous, with vegetation ranging from tall forests with closed canopies to scrublands rich in succulents and thorn-bearing plants (Moro et al., 2015; Paloschi et al., 2020). SDTF foliage patterns are adapted to the intense climate and water seasonality, which is highly dependent on interannual climate variability (Alberton et al., 2017; Medeiros et al., 2022). The vegetation drops most leaves during the dry season, and the first rainfall events trigger a rapid leaf growth in the wet season (Alberton et al., 2017; Paloschi et al., 2020; Medeiros et al., 2022). SDTF are being rapidly degraded (12% between 1980 and 2000), highlighting an urgent priority for their conservation (Moro et al., 2015; Maia et al., 2020). The risks faced by SDTF mainly stem from anthropogenic disturbance effects, which range from local habitat loss to global climate change, leading to biodiversity loss and reductions in biomass (Allen et al., 2017; Maia et al., 2020).

Application of SEB models to estimate evapotranspiration over SDTF has been challenging due to the incompatibility between the existing assumptions of the models and the specificities of these forests. Precipitation seasonality is the primary phenological regulator of SDTF (Moro et al., 2016; Campos et al., 2019; Paloschi et al., 2020), and land-cover patterns show distinct intra- and inter-annual spectral responses (Cunha et al., 2020; Andrade et al., 2021; Medeiros et al., 2022). Therefore, biophysical remotely-sensed variables, such as Normalized Difference Vegetation Index (NDVI) and surface albedo, which are usually used to select the endmembers, exhibit high spatial and temporal variability in SDTF, which causes ET estimates from the SEB models to lack fidelity (Silva et al., 2019). Selection of suitable roughness parameters such as *z0m*, *d0*, and kB^{-1} is important for the correct quantification of the energy balance in SDTF. However, these parameters are more challenging to obtain in SDTF than for evergreen forests, as in addition to vegetation height, other characteristics such as plant density, above-ground plant structure and the strong seasonality of phenology (Alberton et al., 2017; Miranda et al., 2020; Paloschi et al., 2020) have a considerable effect on the turbulent transfer in these forests. Another key issue is how to verify the results of SEB methods due to the scarcity, in many regions, of terrestrial observations and the uneven

148 spatiotemporal distribution of monitoring data. SEB models may not satisfactorily represent ET in
149 regions with sparse vegetation and high climatic seasonality, such as SDTF (Senkondo et al., 2019;
150 Laipelt et al., 2021; Melo et al., 2021). The main reason is that these methods have generally been
151 evaluated and/or parameterized using sites located in other ecosystems and climates in North
152 America, Europe, Australia, East Asia, and in agricultural regions that have characteristics quite
153 distinct from SDTF (Melo et al., 2021). Therefore, a better quantification of ET, especially in regions
154 with high climatic seasonality, will help to design better water management policies that will be able
155 to deal with the effects of climate variability, land use/cover and climate changes (Lima et al., 2021).
156 We hypothesise that a SEB model that improves or considers estimates of *rah* via *z0m* and
157 kB^{-1} will improve *H* and ET for STDF. To test this assumption, we introduce a novel calibration-free
158 SEB model based upon a one-source bulk transfer equation, herein referred to as Seasonal Tropical
159 Ecosystem Energy Partitioning (STEEP). The STEEP model aims to improve *H* and ET estimates
160 for STDF by incorporating the woody structure of plants through the Plant Area Index (PAI), and soil
161 moisture obtained by remote sensing to help represent the seasonality of the aerodynamic and
162 surface variables that drive the energy fluxes. To obtain the coefficients of the linear relationship
163 between *dT* and LST its coefficients, we computed *H* by the surface energy balance, and the
164 remaining λET through the principle of the Priestley-Taylor equation in the hot/dry and cold/wet
165 endmembers. STEEP is designed to take advantage of the extensive free database available on the
166 Google Earth Engine (GEE) cloud computing environment. STEEP is herein evaluated at the field
167 scale against four flux towers in the Caatinga, the largest continuous SDTF in the Americas.
168 Additionally, the model was compared with SEBAL and two consolidated global ET products: MOD16
169 (Mu et al., 2011; Running et al., 2017) and PMLv2 (Zhang et al., 2019).
170
171 **2. Methodology**
172 2.1 Study areas and respective data
173 The study concerns the Brazilian Caatinga, located between the Equator and the Tropic of
174 Capricorn (about 3 and 18° south), in the Brazilian semiarid region. It covers an area of about
175 850,000 km² (Silva et al., 2017a; Andrade et al., 2021; Brazil MMA, 2021). The climate in the
176 Caatinga is characterized by high air temperatures (around 26–30° C) and high potential

evapotranspiration (1,500–2,000 mm/year) coupled with low annual rainfall (300–800 mm/year, normally concentrated in 3–6 months) with high intra- and inter-annual variability in space and time, and a long dry season which sometimes lasts up to 11 months in some areas of Caatinga (Moro et al., 2016; Miranda et al., 2018; Paloschi et al., 2020). The Caatinga vegetation has at least thirteen physiognomies ranging from woods to sparse thorny shrubs, morphologically adapted to resist water stress and high air temperatures (Araújo et al., 2009; Silva et al., 2017a; Marques et al., 2020; Miranda et al., 2020), and it has been identified as one of the most biodiverse SDTF regions globally (Pennington et al., 2006; Santos et al., 2014; Koch et al., 2017). Still, the Caatinga and other SDTF are among the least studied ecoregions compared to tropical forests and savannas (Santos et al., 2012; Koch et al., 2017; Tomasella et al., 2018; Borges et al., 2020). Only 1% of the Brazilian Caatinga area is legally protected (Koch et al., 2017).

We used data from four sites located in the Caatinga (Fig. 1 and Table 1). The surrounding areas of each of our study sites — which exceeds these EC towers footprints — are homogeneously covered by Caatinga vegetation (Fig. S1). Located on crystalline terrain (Fig. 1a), these Caatinga sites have soils with highly variable properties, ranging from fertile (those with a clayey texture) to poor (those soils that are sandier). However, most soils of the SDTF are typically shallow and stony (i.e. Entisols, Alfisols, and Ultisols; WRB, 2006), retaining water only for a short period between rainfall events and after the rainy season (Moro et al., 2015; Queiroz et al., 2017). The wet and (dry) seasons from the sites Petrolina (PTN) are concentrated in Jan–Apr (May-Dec; Souza et al., 2015); Serra Negra do Norte (SNN) in Jan–May (June–Dec; Marques et al., 2020); Serra Talhada (SET) in Nov–Apr (May–Oct; Silva et al., 2017b) and Campina Grande (CGR) in Mar–July (Aug–Feb; Oliveira et al., 2021). The climate of the four observation sites is semi-arid, type BSh (Fig. 1b) according to the Köppen climate classification (Alvares et al., 2013).

Eddy covariance data, covering several periods from 2011 to 2020 (Fig. 1c), were used to evaluate the modelled ET and *H*. The four sites were instrumented with five flux towers equipped with three-dimensional ultrasonic anemometers (CSAT3, Campbell Scientific Inc., Logan, UT, USA in all the sites except CGR 2020) and open-path infrared gas analysers (LI-7500, LI-COR Inc., Lincoln, NE, USA, in the PTN site, or EC150, Campbell Scientific Inc., Logan, UT, USA, in the SET, SNN, and CGR 2014 sites). In the more recent experiment (CGR 2020), the flux tower was equipped

with an IRGASON (Campbell Scientific Inc., Logan, UT, USA) that integrates the two sensors in just one instrument. ET data for the PTN, SNN, and SET sites have been previously described; they underwent standard procedures to ensure their quality and were published by Melo et al. (2021). Observations at the CGR site were collected through two micrometeorological towers, located in a dense Caatinga area within the Brazilian National Institute of Semiarid (INSA) experimental area, a 300 ha forest reserve with different stages of regeneration. The first tower (height of 7 m) was active between the years of 2014 and 2017, as described in Oliveira et al. (2021). The second tower (height of 15 m) is part of the Caatinga Observatory (OCA) and includes an EC system that has been collecting data since 2020. The OCA is a laboratory maintained by the Federal University of Campina Grande and INSA. *H* data for the PTN, SNN and CGR sites have been obtained from the respective principal investigators, while data for the SET site have been obtained from the AmeriFlux network (Antonino, 2019). For the retrieval of λET and *H*, LoggerNet software (Campbell Scientific, Inc., Logan, UT, USA) was used in order to transform 10 Hz raw data into 30 min binaries. Afterwards, EdiRe software (Campbell Scientific Inc., Logan, UT, USA) was used to process the high-frequency data, averaging every 30 min. The data from the EC flow towers in CGR have previously gone through standard procedures to ensure their quality. Detailed information on data processing, quality control, and post-processing can be found in Campos et al. (2019) and Cabral et al. (2020). The raw data from the CGR flux tower were processed by Easy-flux data processing software (Campbell Scientific Inc., Logan, UT, USA). In addition, data for any day with rainfall greater than 0.5 mm were removed. The daily ET was calculated using the daily average λET.

232 Table 1. List of EC-equipped flux tower observation sites in the study area.

Sites	State of Brazil	Mean annual of rainfall (mm)[1]	Site average elevation (m)	Main tree species	Location (Lon;Lat)	Data availability	Wet / Dry Seasons	Main reference
Petrolina (PTN)	Pernambuco	428.6	395	*Commiphora leptophloeos, Schinopsis brasiliensis, Mimosa tenuiflora, Cenostigma microphyllum, Sapium glandulosum*	-40.3212; -9.0465	Jan–Dec 2011	Jan-Apr / May-Dec	Souza et al. (2015)
Serra Negra do Norte (SNN)	Rio Grande do Norte	629.5	205	*Caesalpinia pyramidalis, Aspidosperma pyrifolium, Anadenanthera colubrina, Croton blanchetianus*	-37.2514; -6.5783	Jan–Dec 2014	Jan-May / June-Dec	Marques et al. (2020)
Serra Talhada (SET)	Pernambuco	648	465	*Mimosa hostilis, Mimosa verrucosa, Croton sonderianus, Anadenthera macrocarpa, Spondias tuberosa*	-38.3842; -7.9682	Jan–Dec 2015	Nov-Apr / May-Oct	Silva et al. (2017b)
Campina Grande (CGR)	Paraíba	777	490	*Croton blanchetianus, Mimosa ophthalmocentra, Poincianella pyramidalis, Allophylus quercifolius, Mimosa sp.* [2]	-35.9750; -7.2798	Jan–Dec 2014	Mar-July / Aug-Feb	Oliveira et al. (2021)
Campina Grande (CGR)	Paraíba	777	490	*Croton blanchetianus, Mimosa ophthalmocentra, Poincianella pyramidalis, Allophylus quercifolius, Mimosa sp.* [2]	-35.9763; -7.2805	Jan–Dec 2020	Mar-July / Aug-Feb	This study

[1] Rainfall Data Sources: Brazilian National Institute of Meteorology (INMET) and Pernambuco State Agency for Water and Climate (APAC).

[2] Barbosa et al. (2020).

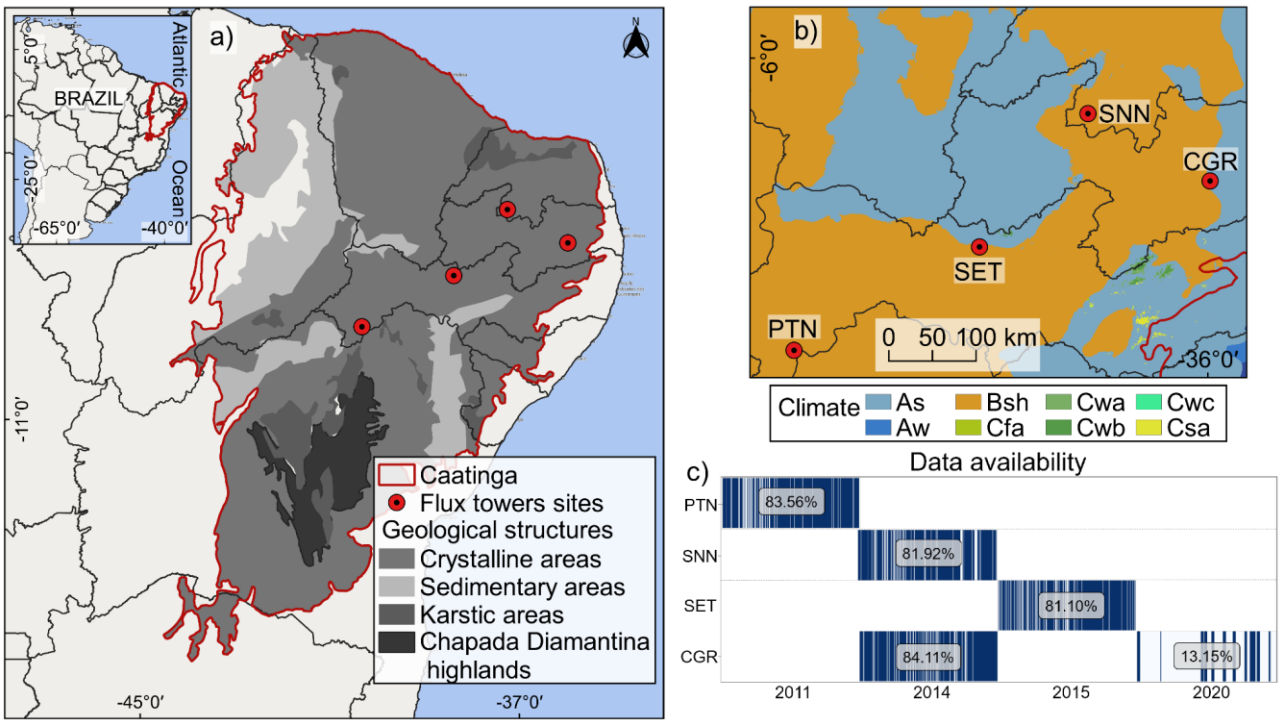

Fig. 1. Location of flux tower observation sites in Caatinga. a) Geographical overview of the Caatinga (Moro et al., 2015), b) Köppen's climate classification map:Tropical zone with dry summer (As), Tropical zone with dry winter (Aw), Dry zone semi-arid low latitude and altitude (Bsh), Humid subtropical zone without dry season and with hot summer (Cfa), Humid subtropical zone with dry winter and hot summer (Cwa), Humid subtropical zone with dry winter and temperate summer (Cwb), Humid subtropical zone with dry winter and short and cool summer (Cwc), Humid subtropical zone with dry summer and hot (Csa), according to Alvares et al. (2013) and c) Data availability on the observation sites after procedures to ensure their quality.

2.2 The Seasonal Tropical Ecosystem Energy Partitioning (STEEP) model

SEB models have been applied in many parts of the world (Mohan et al., 2020a). The one-source SEB models that are most commonly found in the literature are SEBAL (Bastiaanssen et al., 1998), Surface Energy Balance System (SEBS; Su, 2002), Mapping EvapoTranspiration at high Resolution with Internal Calibration (METRIC; Allen et al., 2007), and Operational Simplified Surface Energy Balance (SSEBop; Senay et al., 2013). As in other SEB models, STEEP performs the energy balance at the time of satellite overpass (instantaneous) to obtain λET as the surface energy balance residual. The computation of R_n and G, necessary to get λET, followed the procedures described in Ferreira et al. (2020) and Bastiaanssen et al. (2002), respectively, but with input data from the

253 Moderate-Resolution Imaging Spectroradiometer (MODIS) sensor. *H* was calculated following the
254 methods described in Table 2: using *rah* and *dT*, both traditionally applied in SEB models, but also
255 focusing on peculiarities of SDTF that have never been considered in other SEB models. In this
256 proposed version, *rah* was described according to Verhoef et al. (1997a) and Paul et al. (2013),
257 which requires, among other parameters/variables, the momentum roughness length (*z0m*), the zero
258 plane displacement height (*d0*), the dimensionless parameter kB^{-1}, and the atmospheric stability
259 corrections (Paulson, 1970). *z0m* is influenced by a range of plant structural properties, e.g.
260 vegetation height, breadth and vegetation drag coefficients, and spacing (or density). *z0m* is
261 commonly computed as a function of Leaf Area Index (LAI; Verhoef et al., 1997b; Liu et al., 2021).
262 However, most SDTF plants spend a substantial part of the year without leaves; under these
263 conditions, *z0m* should be derived from information on dimensions of trunks, stems, and branches.
264 Since LAI is only related to leaf cover quantity and variability, it cannot represent the woody plant
265 structure without leaves (Miranda et al., 2020). Therefore, the Plant Area Index (PAI), which is the
266 total above-ground plant area, i.e. leaves and woody structures, was used to represent plant
267 structures in the computation of *z0m* and *d0*.

268 To incorporate the conditions of water variability in the forest system in the calculation of
269 sensible heat we applied the procedure described in Gokmen et al. (2012) that corrects the kB^{-1}
270 equation presented in Su et al. (2001), incorporating soil moisture obtained by remote sensing. The
271 canopy conductance profiles are the link between soil moisture and sensible/latent heat flux. The
272 source of sensible/latent heat moves vertically throughout the canopy as a function of plant water
273 stress (Gokmen et al., 2012; Bonan et al., 2021), which affects heat roughness length, and, therefore,
274 kB^{-1} and *rah*. Thus, when there is a reduction in soil moisture, there is also a reduction in the value
275 of *rah* and, consequently, an increase of *H* and a decrease in λET. Furthermore, to calculate *dT*, we
276 used the linear relationship on LST, using the assumption of extreme contrast in terms of cover and
277 soil wetness (hot/dry and cold/wet endmembers) to determine the linear relationship coefficients.
278 However, in the hot/dry and cold/wet endmembers pixels, *H* was computed by the surface energy
279 balance (Allen et al., 2007), and the remaining λET was incorporated through the Priestley-Taylor
280 (1972) equation and plant physiological constraints following the approach in Singh and Irmak (2011)
281 and French et al. (2015). PAI and soil moisture time series used in our study can be seen in Fig. S2.

The references for the methods and equations adopted to formulate the STEEP model can be found in Table 2 and Appendix A, respectively. For illustration purposes, Table 2 also shows the references for the methods for one of the most widely used RS SEB models, the SEBAL model.

Table 2. References for the methods used in the STEEP and SEBAL models to obtain the sensible heat flux.

Variable/Parameter	STEEP	SEBAL
Aerodynamic resistance for heat transfer (*rah*)	Verhoef et al., 1997a; Paul et al., 2013	Bastiaanssen et al., 2002; Laipelt et al., 2021
Roughness length for momentum transfer (*z0m*)	Verhoef et al., 1997b; Paul et al., 2013, replacing LAI with PAI	Bastiaanssen et al., 2002; Laipelt et al., 2021
Zero plane displacement height (*d0*)	Verhoef et al., 1997b; Paul et al., 2013	-
Plant Area Index (PAI)	Miranda et al., 2020	-
Parameter kB^{-1}	Su et al., 2001	uses *z0h* with constant value (0.1); Bastiaanssen et al., 2002
Correction of soil moisture by remote sensing in kB^{-1}	Gokmen et al., 2012	-
Calculation of the *H* and the remaining λET in endmembers pixels	Allen et al., 2007; Singh and Irmak, 2011; French et al., 2015	Calculation of the *H* in the hot/dry endmember only; Bastiaanssen et al., 2002

2.3 Algorithm implementation and processing

We implemented STEEP on the Google Earth Engine (GEE) cloud computing environment (Gorelick et al., 2017) using the Python API (version 3.6). Statistical analyses to evaluate the performance of the models were also conducted in Python and implemented in the Jupyter programming environment. The Python package geemap (Wu, 2020) enabled the integration of Python with the GEE environment, and the hydrostats package (Roberts et al., 2018) was used for the statistical evaluation of the performance of the models.

We designed the application of the model to take advantage of the data available on GEE (Table 3). The remote sensing datasets were derived from MODIS sensor products, the Shuttle Radar Topography Mission (SRTM; Farr et al., 2007), and the Global Forest Canopy Height product provided vegetation height (Potapov et al., 2021). The climate data necessary to run the model, i.e. wind speed, air temperature, relative humidity, shortwave radiation, and net thermal radiation at the surface, were sourced from the ERA5-Land reanalysis product (Muñoz Sabater, 2019). For data

regarding soil moisture, we used the Global Land Data Assimilation System (GLDAS) product (Rodell et al., 2004). CHIRPS precipitation product (Funk et al., 2015) was used to estimate the daily rainfall amount at the sites evaluated.

Table 3. Description of the datasets available on the GEE platform used in the research.

Product	GEE ID	Bands/variables	Time coverage	Spatial resolution	Temporal resolution
MCD43A4.006	MODIS/006/MCD43A4	B1–B7	Feb 2000–present	0.5 km	1 day
MOD09GA.006	MODIS/006/MOD09GA	SolarZenith	Feb 2000–present	1 km	1 day
MOD11A1.006	MODIS/006/MOD11A1	LST_Day_1km; Emis_31, Emis_32	Mar 2000–present	1 km	1 day
SRTM	USGS/SRTMGL1_003	Elevation	Feb 2000	0.03 km	-
ERA5-Land	ECMWF/ERA5_LAND/HOURLY	dewpoint_temperature_2m, temperature_2m, u_component_of_wind_10, v_component_of_wind_10m, surface_net_solar_radiation_hourly, surface_net_thermal_radiation_hourly	Jan 1981–present	0.1°	1 h
GLDAS	NASA/GLDAS/V021/NOAH/G025/T3H	SoilMoi0_10cm_inst	Jan 2000–present	0.25°	3 h
Global Forest Canopy Height, 2019	users/potapovpeter/GEDI_V27	-	Apr 2019	0.03 km	-
CHIRPS	UCSB-CHG/CHIRPS/DAILY	Precipitation	Jan 1981–present	0.05°	1 day
MOD16A2.006	MODIS/006/MOD16A2	ET	Jan 2001–present	0.5 km	8 days
PML_V2	projects/pml_evapotranspiration/PML/OUTPUT/PML_V2_8day_v016	Es, Ec, Ei	Feb 2000–present	0.5 km	8 days

The presence of clouds or instrumental malfunctioning of orbital sensors can cause gaps in data. To reduce the loss of information due to missing data, we chose to use the MODIS MCD43A4

reflectance product. By combining reflectance data from MODIS sensors aboard the AQUA and TERRA satellites and modelling the anisotropic scattering characteristics using sixteen-day quality observations, the MCD43A4 product represents the daily dynamics of the Earth's surface without missing data (Schaaf and Wang, 2015). Daily surface reflectance data from the MCD43A4 product were used to obtain the surface albedo and vegetation indices (NDVI and PAI) needed to run STEEP. Thus, the surface albedo data and the vegetation indices show a low percentage of missing data. To compose the LST time series, we used data from MOD11A1, and to fill its missing data, a filter with the average value for a monthly window was applied. This procedure is similar to the method proposed by Zhao et al. (2005) and it is also used by the MOD16 algorithm to generate the continuous global ET (Mu et al., 2011).

Following the approach in comparable studies, STEEP algorithm processing was conducted with automatic selection of endmembers pixels (Bhattarai et al., 2017; Silva et al., 2019; Laipelt et al., 2021). Like Silva et al. (2019), we used the biophysical variables NDVI, surface albedo and LST to automate selection of the endmembers, but we applied different criteria. For the hot/dry endmember selection, the first step consisted of selecting those pixels whose surface albedo values are between the 50 and 75% quantiles, and with NDVI values greater than 0.1 and less than the 15% quantile. After this first selection, a refinement is applied by selecting only those pixels from this first set that have LST values between the 85 and 97% quantiles. Using the set of pixels that met these criteria, the median values of R_n, G, LST and *rah* were calculated to establish a single value for each variable and describe the characteristics of the hot pixel. We applied a similar procedure to select the cold/wet endmember but with different limits (Table 4). The procedure for finding endmembers was conducted daily. To execute the model and conduct the selection of endmembers, we used an area of interest (AOI), also known as domain size. AOI was defined as a square area with 1000-km sides within the Caatinga domain and centred on the tower coordinates of each site. Cheng et al. (2021), for example, applied the SEBAL using MODIS data in China and used an AOI of 1200-km x 1200-km.

Table 4. Methodology used for the selection of endmembers pixels.

Endmembers

	Hot/dry pixel	Cold/wet pixel
Step 1	Q50% < surface albedo < Q75% and 0.10 < NDVI < Q15%	Q25% < surface albedo < Q50% and NDVI > Q97%
Step 2	of the pixels of the 1st Step, select pixels with Q85% < LST < Q97%	of the pixels of the 1st Step, select pixels with LST < Q20%
Step 3	Of the set of pixels that met the previous steps, the median values of R_n, G, LST and *rah* were calculated to establish a single value for each variable and describe the characteristics of endmembers	

Q = quantile.

2.4 Analysis of the algorithms' performance

We used SEBAL as a reference RS SEB model for comparison with STEEP. SEBAL is one of the most applied SEB models since the algorithm uses a minimal number of in situ measurements compared to similar models, e.g. METRIC and SSEBop, and is considered a suitable choice for evapotranspiration estimates over cropped areas and in the context of water resource management (Kayser et al., 2022). Applications with SEBAL have been conducted in the Caatinga as in the studies of Teixeira et al. (2009), Santos et al. (2020), Costa et al. (2021), and Lima et al. (2021). Implementations of the SEBAL algorithm are popular on several computing platforms, e.g. GRASS-Python (Lima et al., 2021); Google Earth Engine (Laipelt et al., 2021); Python (Mhawej et al., 2020), following the formulations described in Bastiaanssen et al. (1998) and Bastiaanssen et al. (2002). The SEBAL version implemented in this work followed those presented by Bastiaanssen et al. (2002), Costa et al. (2021) and Laipelt et al. (2021). The remote sensing datasets and endmembers pixels selection for SEBAL were the same as described in STEEP.

ET and *H* estimates from STEEP and SEBAL were evaluated against the eddy covariance measurements of the corresponding tower. Here, the modelled values were extracted for the pixel representing the EC tower for each observation site. The footprint fetches for PTN, SET, SNN is less than 500 m (Silva et al., 2017b; Campos et al., 2019; Santos, et al., 2020). We assume a similar footprint for CGR due to its similarity in terms of wind characteristics and terrain slope compared to the other sites. Moreover, the surrounding areas of each of our study sites (Fig. S1) — which exceeds these EC towers footprints — are homogeneously covered by Caatinga vegetation. We evaluated daily ET values, and instantaneous hourly *H* values more specifically with the modelled/measured *H*

357 value at 11:00 am local time (GMT-3), considering this is the closest time to the satellite's overpass.
358 Additionally, the STEEP model was compared with two consolidated global ET products available
359 on GEE: MODIS Global Terrestrial Evapotranspiration A2 version 6 (MOD16; Mu et al., 2011;
360 Running et al., 2017) and Penman-Monteith-Leuning model version 2 global evaporation (PMLv2;
361 Zhang et al., 2019); both products have a pixel resolution of 500 m (Table 3). The algorithm used in
362 MOD16 is based on the Penman-Monteith equation and driven by MODIS remote sensing data with
363 Modern-Era Retrospective analysis for Research and Applications (MERRA; Mu et al., 2011). In
364 MOD16 ET is the sum of soil evaporation (Es), canopy transpiration (Tc) and wet-canopy evaporation
365 (Ec) and is provided as eight-day *cumulative* values. More details about MOD16 can be found in Mu
366 et al. (2011) and Running et al. (2017). The global PMLv2 product involves a biophysical model
367 based on the Penman-Monteith-Leuning equation which also uses MODIS remote sensing data, but
368 with meteorological reanalysis data from GLDAS as model inputs. As in MOD16, ET in PMLv2 is
369 also the sum of Es, Tc and Ec but is provided as eight-day *average* values. To make MOD16 and
370 PMLv2 values compatible, ET of PMLv2 was multiplied by eight. Details about PMLv2 can be found
371 in Gan et al. (2018) and Zhang et al. (2019). We accumulated the daily ET measured at the
372 observation sites, i.e. derived from EC data, and ET modelled with STEEP for the same eight-day
373 time periods to make them compatible with the temporal resolution of the MOD16 and PMLv2
374 datasets. The average of the measured daily values over each eight-day time period (even if there
375 were missing values within this period) was multiplied by eight to calculate the observed 8-day ET.
376 To match the time steps of STEEP and MOD16/PMLv2 ET values, the 8-day average of the
377 evaporative fraction (EF) was multiplied by the daily net radiation over those 8 days, assuming that
378 EF can be considered constant in each of these periods. Then the ET was summed over the 8-day
379 interval. Finally, we also compared the modelled ET (by STEEP and the two global products) with
380 the observed ET, only in the 8-day periods when no field-observed data was missing. However, with
381 this criterion the number of observations dropped dramatically.
382 The STEEP and SEBAL models and global ET products were evaluated with five performance
383 metrics (Table 5). A combination of performance metrics is often used to assess the overall
384 performance of models because a single metric provides only a projection of a certain aspect of the
385 error characteristics (Chai and Draxler, 2014). Root mean square error (*RMSE*) is commonly used

to express the accuracy of the results with the advantage that it presents error values in the same units of the variable analysed; optimal values are close to zero (Hallak and Pereira Filho, 2011). Coefficient of determination (R^2) represents the quality of the linear trend between observed and simulated data and ranges from 0 to 1; high values indicate better model performance. Nash–Sutcliffe efficiency (*NSE*) indicates the accuracy of the model output compared to the average of the referred data (*NSE* = 1 is the optimal value; Nash and Sutcliffe, 1970). Concordance correlation coefficient (*ρc*) is a measure that evaluates how well bivariate data falls on the 1:1 line. *ρc* measures both precision and accuracy. It ranges from -1 to +1 similar to Pearson's correlation coefficient, with perfect agreement at +1 (Lin, 1989; Liao and Lewis, 2000; Akoglu, 2018). Percentage bias (*PBIAS*) measures the average relative difference between observed and estimated values, with an optimal value of 0 (Gupta et al., 1999). Additionally, we evaluate STEEP's model structure by extracting model's performance metrics after excluding it from its main implementations individually (Table 2) and by two-by-two combinations of *z0m*, *rah* and *rλET*. We run the control version of the SEB model, i.e. SEBAL in our case, while incorporating one or two improvements in the model and keeping the remaining parts of the algorithm the same as the reference SEB model.

Table 5. Performance metrics used to evaluate ET and *H* in this study.

Performance metric	Equation	Range (Perfect value)
Root mean square error (*RMSE*)	$RMSE = \sqrt{\frac{\sum_{i=1}^{N}(M_i - O_i)^2}{N}}$	[0, +∞ [(0)
Coefficient of determination (R^2)	$R^2 = \frac{\left[\sum_{i=1}^{N}(O_i - \bar{O})(M_i - \bar{M})\right]^2}{\sum_{i=1}^{N}(O_i - \bar{O})^2 \cdot \sum_{i=1}^{N}(M_i - \bar{M})^2}$	[0, 1] (1)
Nash–Sutcliffe efficiency (*NSE*)	$NSE = 1 - \frac{\sum_{i=1}^{N}(M_i - O_i)^2}{\sum_{i=1}^{N}(O_i - \bar{O})^2}$	]-∞, 1] (1)
Concordance correlation coefficient (*ρc*)	$\rho c = \frac{2\sum_{i=1}^{N}(O_i - \bar{O})(M_i - \bar{M})}{\sum_{i=1}^{N}(O_i - \bar{O})^2 + \sum_{i=1}^{N}(M_i - \bar{M})^2 + (N-1)(\bar{O} - \bar{M})^2}$	[-1, 1] (1)
Percentage bias (*PBIAS*)	$PBIAS = \frac{\sum_{i=1}^{N}(M_i - O_i) \cdot 100}{\sum_{i=1}^{N} O_i}$	]-∞, +∞ [(0)

where: *N* sample size; O observed value; M modelled value; $\bar{O}$ observed mean; $\bar{M}$ modelled mean.

3. Results and discussion

3.1 Comparison of STEEP and SEBAL models results with observed (EC) values

The performance statistics of daily ET by STEEP and SEBAL in wet and dry seasons for the evaluated sites are shown in Fig. 2. In general, STEEP exhibited a better performance than SEBAL. Although the better statistical metrics of STEEP were in the dry season, in the wet season, they were also superior compared to SEBAL. Specifically, in the dry season, STEEP exhibited a *RMSE* between 0.6 and 1.06 mm/day, while SEBAL this was between 1.06 and 2.24 mm/day. The maximum value of R^2 in STEEP was 0.62 (sites PTN and SNN), whereas SEBAL achieved only 0.33. The *NSE* metric was the worst among the five analysed in SEBAL: values lower than -7.5 occurred in three of the five sites. Although in STEEP, PTN and SNN sites *NSE* had values higher than 0 (0.55 and 0.25, respectively) the other sites also had negative values, reaching up to -2.5. In terms of ρc, values ranged from 0.09 to 0.77 in STEEP and from -0.04 to 0.41 in SEBAL. It is also possible to see the reduction that STEEP has brought to ET modelling in terms of *PBIAS* when compared to SEBAL.

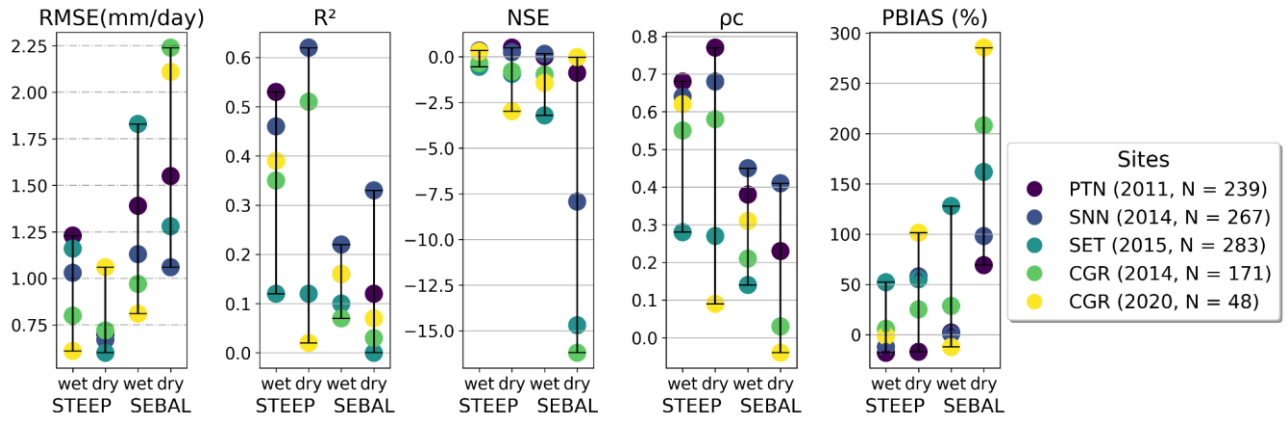

Fig. 2. Results of the performance statistics of daily ET in wet and dry seasons for evaluated sites.

Globally, without discriminating between wet and dry seasons, STEEP exhibited better statistical performance than SEBAL at all the evaluated sites (Fig. 3). While STEEP exhibited a *RMSE* between 0.75 and 0.94 mm/day, the *RMSE* for SEBAL was between 1.08 and 1.75 mm/day. In terms of R^2, the values were between 0.24 to 0.69 for STEEP, and were below 0.2 for SEBAL for all sites except in SNN (0.55). Similarly, *NSE* and ρc values were higher for STEEP compared to SEBAL. For STEEP, all sites had *NSE* and ρc values above -0.42 and 0.41, respectively, whereas all sites except SNN had values below these limits for SEBAL. Both models overestimated ET (*PBIAS* > 0), with the exception of the STEEP estimates for the PTN site. The highest overestimation by the STEEP model was less than 60%, whereas in SEBAL it was greater than 140%.

SEBAL metrics concerning the modelled ET were similar to those found in other studies. Laipelt et al. (2021) found R^2 ranging from 0.18 to 0.87 when applying SEBAL and comparing it with data from ten EC towers located in different Brazilian biomes (Amazon, Cerrado, Pantanal, and Pampa). Cheng et al. (2021) obtained R^2 of 0.53–0.77 and *RMSE* of 0.89–1.02 mm/day when comparing estimates from SEBAL and EC towers on different land covers in China. Costa et al. (2021), when applying SEBAL in the Caatinga, found R^2 and *NSE* values of 0.57 and 0.36, respectively. Santos et al. (2020) modelled ET with SEBAL at the SNN site for the 2014–2016 period and obtained R^2 and *RMSE* values of 0.28 and 1.43 mm/day, respectively. For this site, we obtained R^2 and *RMSE* of 0.55 and 1.08 mm/day, respectively, for the year 2014 using SEBAL.

STEEP exhibited a greater seasonal accuracy compared to SEBAL (Fig. 3), as evidenced by the goodness-of-fit between simulated and observed values expressed by the *NSE* indicator. STEEP estimates followed the same temporal evolution as the observed values. STEEP satisfactorily captured both minimum and maximum ET values, including after rainfall events, this is particularly evident in Fig. 3a, where the two observed ET peaks in late 2011 — between DOY 300 and 360 — in the PTN site were captured nicely by STEEP. This improved performance can be explained because soil moisture is incorporated in the STEEP algorithm. In semi-arid regions and particularly in the SDTF, besides the availability of energy, evapotranspiration is highly dependent on the soil–water availability (Lima et al., 2012; Carvalho et al., 2018; Mutti et al., 2019; Paloschi et al., 2020). In rainy months, low daily ET rates are often observed due to the reduced levels of incoming radiation caused by high cloud cover (Mutti et al., 2019; Paloschi et al., 2020). Towards the end of the wet period, when the available energy increases, the daily ET values also increase as a result of the high soil water availability from previous precipitation events (Allen et al., 2011; Marques et al., 2020). In the transition period from the rainy to the dry season, the leaves do not fall immediately (see Table 1, main tree species). Instead, leaf-shedding depends on the environmental conditions in each location, including the rainy season duration, and species composition (Lima and Rodal, 2010; Lima et al., 2012; Miranda et al., 2020; Paloschi et al., 2020; Queiroz et al., 2020; Medeiros et al., 2022). The remaining water available in the soil or previously accumulated in plant tissues is sufficient for the Caatinga vegetation to maintain its leaves, for short periods, at levels similar to the rainy season (Barbosa et al., 2006; Mutti et al., 2019). However, in the dry season, when soil moisture reaches its

lowest levels, the Caatinga vegetation enters a state of dormancy that is accompanied by leaf drop and a drastic reduction of photosynthetic activity (and hence of transpiration) as a strategy to cope with the lack of available soil moisture (Dombroski et al., 2011; Paloschi et al., 2020). This resilience mechanism is typical of xerophytic and/or deciduous species such as those found in the Caatinga (Lima et al., 2012; Mutti et al., 2019; Paloschi et al., 2020), and explains the low rates of ET in the dry season. In contrast, in SEBAL, which does not consider water availability, it was observed that the daily ET followed the course of the daily net radiation throughout the year, especially in the dry period of each of the experimental sites. This is in agreement with the results of Kayser et al. (2022), who pointed out that estimates with SEBAL can be seasonally accurate in locations where the main driver of ET is the available energy. Our results highlight that SEB models such as SEBAL, which are formulated to be mainly dependent on energy availability and do not consider soil and plant water availability, may not satisfactorily represent ET in semi-arid vegetation such as that found in the SDTF (Gokmen et al., 2012; Paul et al., 2014; Melo et al., 2021).

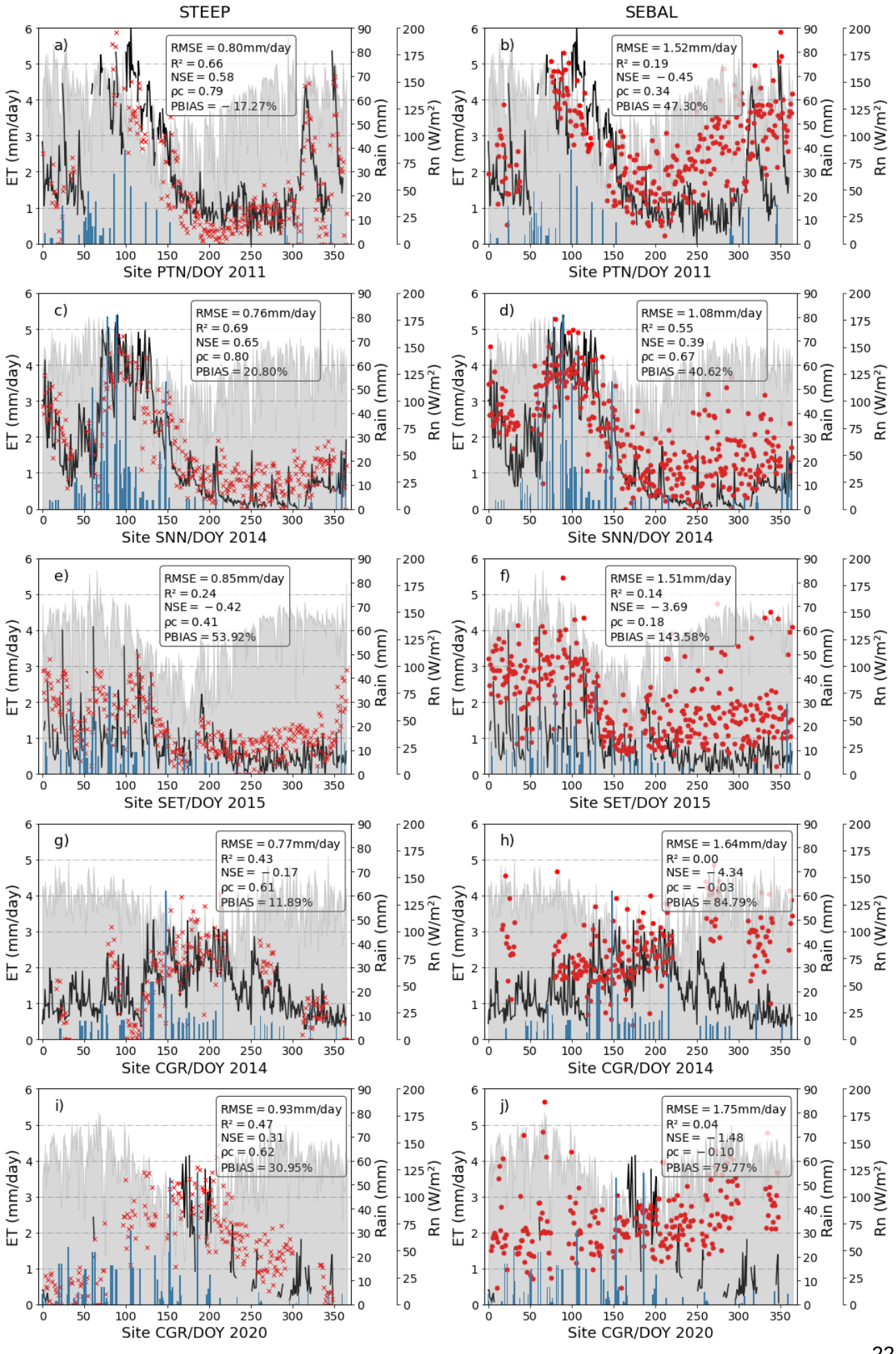
STEEP
SEBAL
a)
RMSE = 0.80mm/day
R² = 0.66
NSE = 0.58
ρc = 0.79
PBIAS = − 17.27%
b)
RMSE = 1.52mm/day
R² = 0.19
NSE = − 0.45
ρc = 0.34
PBIAS = 47.30%
c)
RMSE = 0.76mm/day
R² = 0.69
NSE = 0.65
ρc = 0.80
PBIAS = 20.80%
d)
RMSE = 1.08mm/day
R² = 0.55
NSE = 0.39
ρc = 0.67
PBIAS = 40.62%
e)
RMSE = 0.85mm/day
R² = 0.24
NSE = − 0.42
ρc = 0.41
PBIAS = 53.92%
f)
RMSE = 1.51mm/day
R² = 0.14
NSE = − 3.69
ρc = 0.18
PBIAS = 143.58%
g)
RMSE = 0.77mm/day
R² = 0.43
NSE = − 0.17
ρc = 0.61
PBIAS = 11.89%
h)
RMSE = 1.64mm/day
R² = 0.00
NSE = − 4.34
ρc = − 0.03
PBIAS = 84.79%
i)
RMSE = 0.93mm/day
R² = 0.47
NSE = 0.31
ρc = 0.62
PBIAS = 30.95%
j)
RMSE = 1.75mm/day
R² = 0.04
NSE = − 1.48
ρc = − 0.10
PBIAS = 79.77%
ET (mm/day)
Rain (mm)
Rn (W/m²)
Site PTN/DOY 2011
Site SNN/DOY 2014
Site SET/DOY 2015
Site CGR/DOY 2014
Site CGR/DOY 2020
Observed ET
STEEP
SEBAL
RAIN - CHIRPS
Daily net radiation

470

Fig. 3. Observed and modelled daily evapotranspiration (ET, mm/day) for the different experimental sites: a) and b) PTN 2011, c) and d) SNN 2014, e) and f) SET 2015, g) and h) CGR 2014, i) and j) CGR 2020. The black lines represent observed ET; the red crosses and points are STEEP and SEBAL estimates, respectively; the blue bars represent CHIRPS daily rainfall; the gray region represents daily net radiation from ERA5-land.

The core of the STEEP and SEBAL algorithms is based on finding λET as the residual of the energy balance; however, they differ with regards to the approach used to calculate H. In the STEEP model, the seasonal variation of H fitted the observed values of the instantaneous measurements at 11:00 am (local time) better than SEBAL, for all the sites (Fig. 4). Our results show that an improvement in H leads to a correspondent in ET estimates. This is contrary to the findings of Faivre et al. (2017), who used the same formulation for kB^{-1} applied in our study, but included four different methods to compute $z0m$. While STEEP estimates of H exhibited ρc values over 0.5 for three of the five sites, SEBAL H estimates exhibited ρc values below 0.5 for all sites. When wet and dry seasons data are analysed separately (Fig. 5), the same trend is observed in the results: in general, the STEEP model presents better statistical metrics than SEBAL.

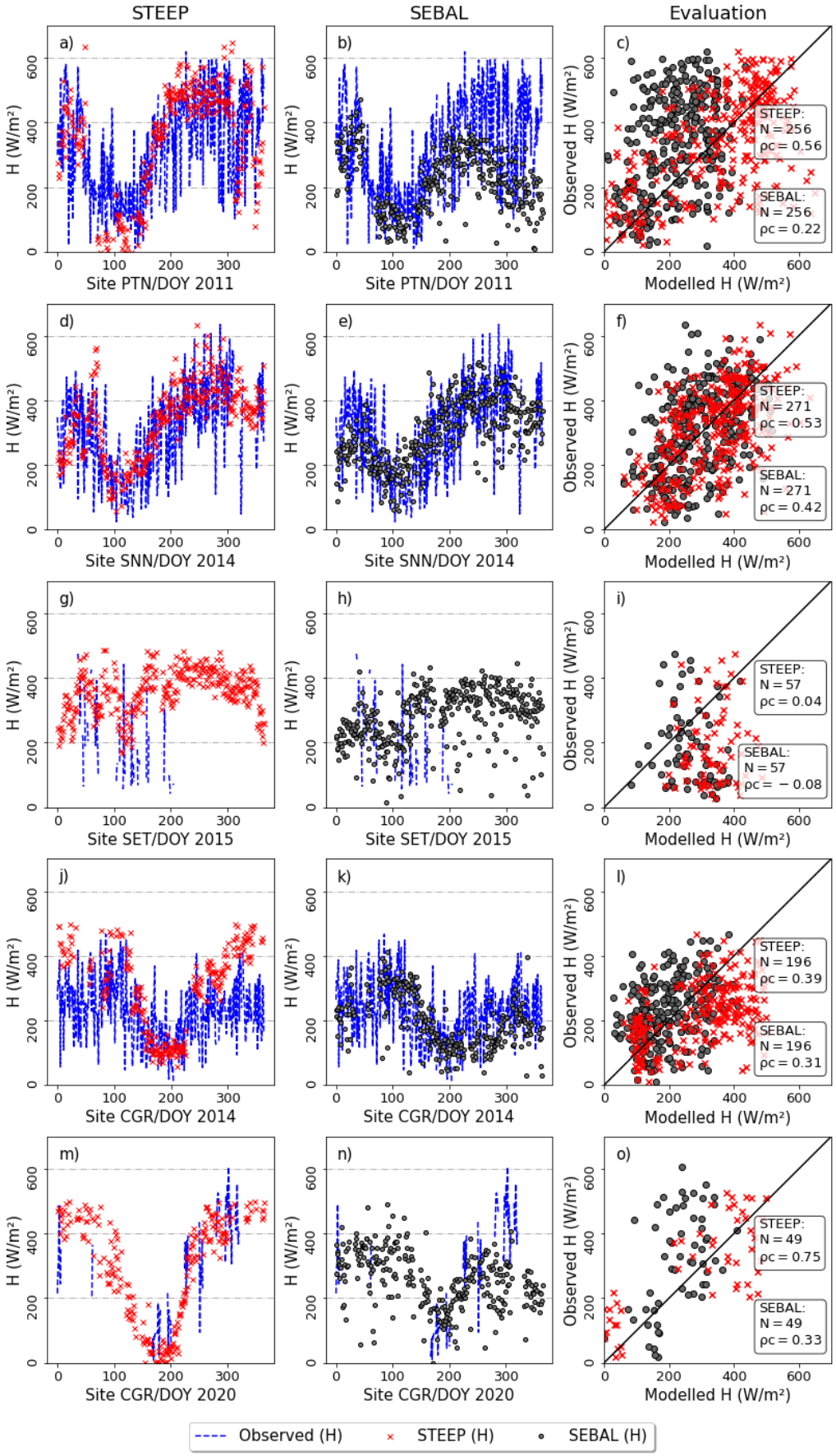

487

488 Fig. 4. Observed and modelled instantaneous sensible heat flux (*H*, at 11:00 am, W/m^2) for the

489 different experimental sites: a), b) and c) PTN 2011, d), e) and f) SNN 2014, g), h) and i) SET

2015, j), k) and l) CGR 2014, m), n) and o) CGR 2020. The blue line represents the observed values; the red crosses and grey points correspond to the STEEP and SEBAL estimates, respectively. The black line is the 1:1 line.

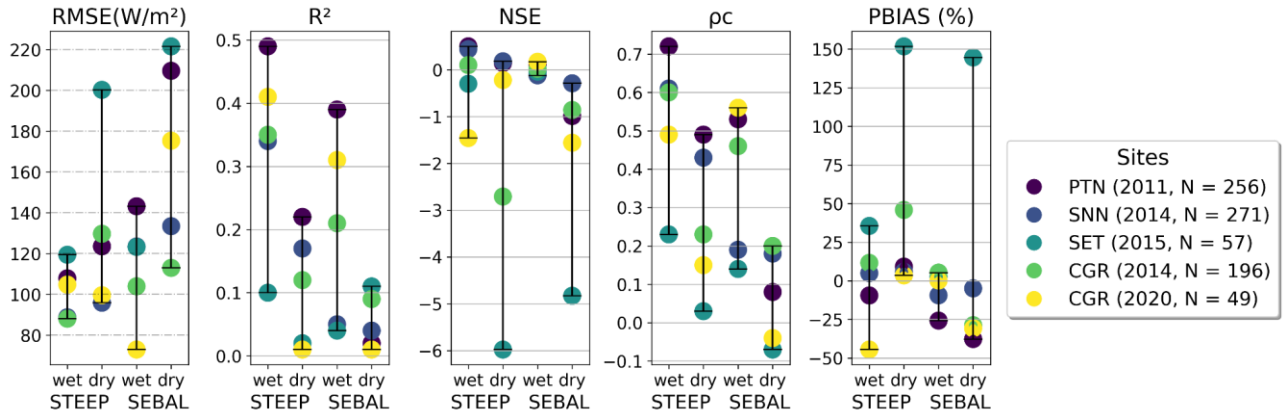

Fig. 5. Results of the performance statistics of instantaneous sensible heat flux (*H*, at 11:00 am, W/m^2) in wet and dry seasons, for the evaluated sites.

Evaluation of the STEEP and SEBAL daily ET and instantaneous *H* for all experimental sites (Fig. 6) indicates that both models lack a high performance for *H* estimates, although the use of STEEP resulted in better statistical measures than when SEBAL was employed (Fig. 6b). This substantiates previous findings (Gokmen et al., 2012; Paul et al., 2014; Trebs et al., 2021), that have shown the tendency of underestimation (overestimation) of H (ET) at water-limited sites. It can be seen that the overestimation of *H* by the STEEP model, compared to SEBAL, produced modelled ET values that were closer to the EC measurements (see Fig. 3 and 4). We ascribe the poor performance of H in the models relative to observed data to the continuous *H* oscillations throughout the day (Campos et al., 2019; Lima et al., 2021). As we compare an instantaneous *H* estimate (STEEP or SEBAL) to the 30-min *H* average measurement (EC), it is expected that modelled *H* performs worse than daily ET for the same site and period. Furthermore, for sites with fewer observations of *H* (SET 2015 and CGR 2020), especially in the dry season, the metrics showed that STEEP did not perform as well, for each season, as other sites with more data available. Still, these limited data were sufficient to show that STEEP outperformed SEBAL in estimating *H*.

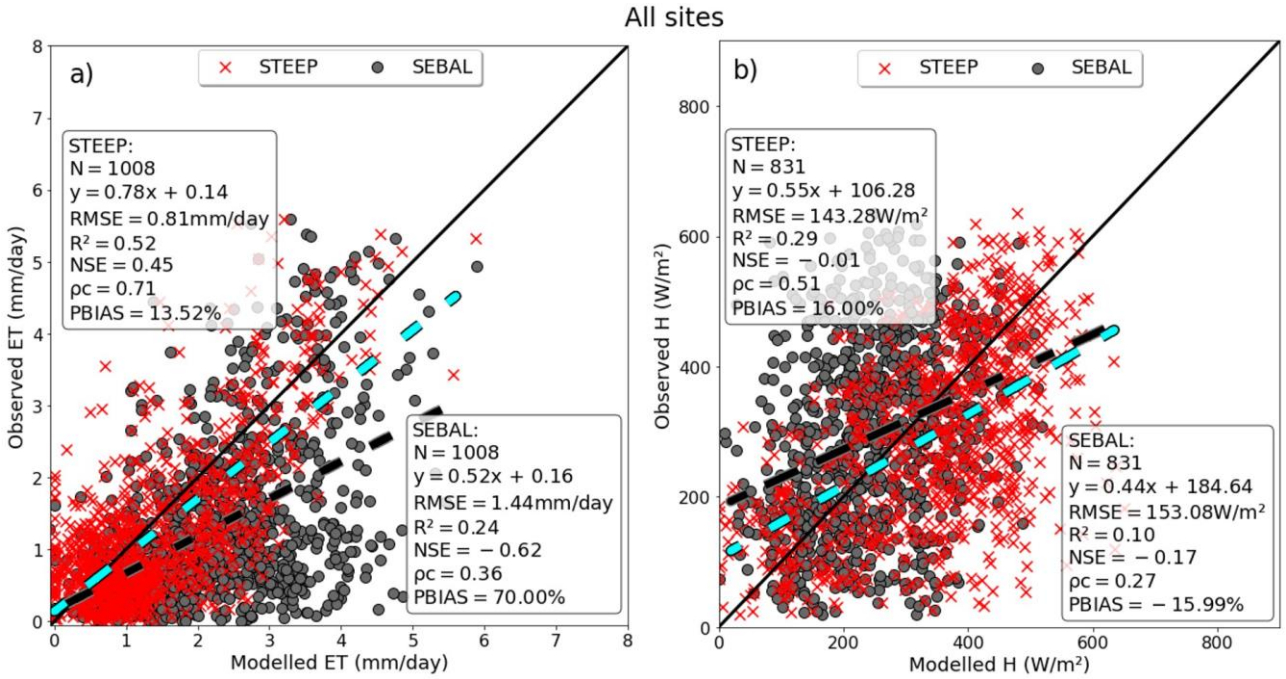

Fig. 6. Evaluation of observed and modelled: (a) daily evapotranspiration (ET, mm/day) and b) instantaneous sensible heat flux (*H*, at 11:00 am, W/m^2) for all experimental sites. STEEP (red crosses) and SEBAL (black points). The black line is the 1:1 line; the cyan (black) dashed line is the fitted linear regression between observed and STEEP (SEBAL) model values.

We attribute the better performance of STEEP over SEBAL for the Brazilian Caatinga to at least three reasons, shown in order of impact of model implementation on its performance (Fig. 7 and Table S1). First, by quantifying the remaining *λET* in the endmembers pixels through the Priestley-Taylor equation, a more reliable estimate of *H* in the endmembers pixels can be obtained, as was also evidenced by Singh and Irmak (2011). This process is critical for the subsequent numerical calculation of *H* in SEB models that use *dT*, as its accuracy is closely related to quantifying the energy balance at the hot and cold endmembers (Trezza, 2006; Allen et al., 2007; Singh and Irmak, 2011; Singh et al., 2012). Secondly, roughness characteristics near the surface where the heat fluxes originate are parameterised by *z0m*, which depends on several factors, such as wind direction, height and type of the vegetation cover (Kustas et al., 1989b). Estimation of *z0m* only with an exponential relationship, as a function of vegetation indices, may be an oversimplification (Kustas et al., 1989a; Paul et al., 2013). In our study, *z0m* and *d0* are calculated with the equations and coefficients proposed in Raupach (1994) and Verhoef et al. (1997b), and using PAI because this

index better represents the intra-annual phenological changes in the Caatinga (Miranda et al., 2020). This procedure considers the characteristics of SDTF, such as seasonality of phenology and vegetation height, that considerably affect the quantification of turbulent transfer (Liu et al., 2021). Third, our study uses the equation described in Verhoef et al. (1997a) and Paul et al. (2013) to estimate *rah*, which considers the differences between heat and momentum transfer, unlike the original equation employed in other SEB models e.g. SEBAL or METRIC that only considers *z0m* and sets *z0h* = 0.1 when computing this resistance. Furthermore, we account for the kB^{-1} parameter that varies in space and time and incorporates the soil moisture content obtained by RS (Su et al., 2001; Gokmen et al., 2012). ET estimation is best represented with a spatially varying kB^{-1} values, as pointed out by the studies of Gokmen et al. (2012) and Paul et al. (2014). Long et al. (2011) report that the introduction of these fixed values (*z0h* or kB^{-1}) has a significant impact on the magnitudes of the estimates of H. Furthermore, Mallick et al. (2018) and Trebs et al. (2021) indicate that the parameterization of *rah* can influence the estimation of ET, especially in SEB models that are largely dependent on *rah*. Our results show that including just one or two of the refinements had only partial performance gains (Fig. 7 and Table S1). In contrast, all the proposed STEEP improvements when implemented together resulted in the best performance metrics for all sites.

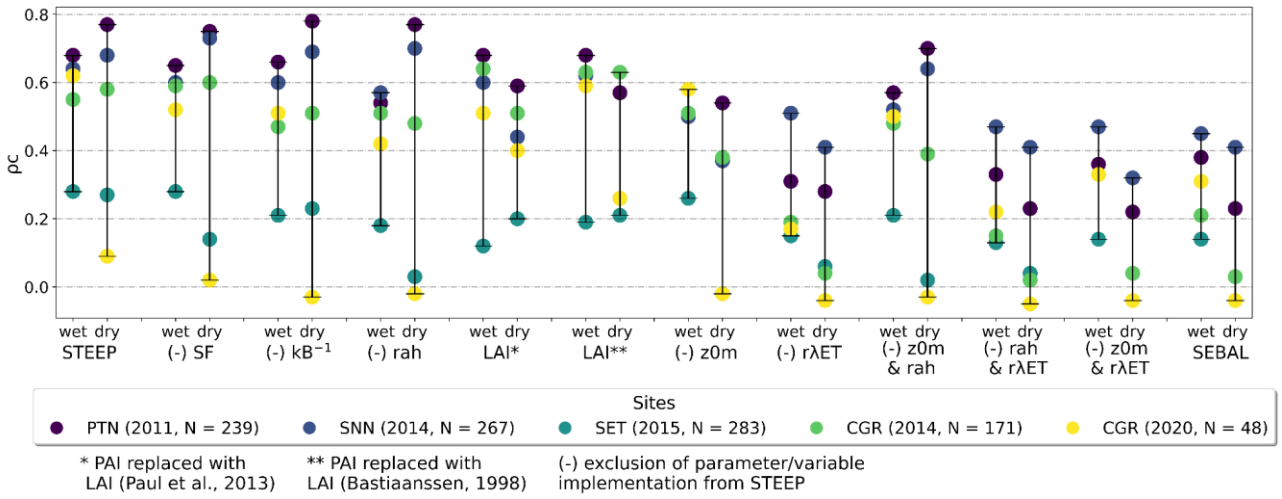

Fig. 7. Change of the concordance correlation coefficient (ρc) by the exclusion/modification of one or two parameters/variables implemented in the STEEP model, in the wet and dry seasons: scale factor soil moisture correction (SF), the parameter kB^{-1}, the aerodynamic resistance for heat transfer (*rah*), PAI replace with LAI (determined by two different methods), the roughness length for momentum transport (z0m) and the residual latent heat flux in the end members pixels (*rλET*).

3.2 Comparison of STEEP model estimates with global evapotranspiration products

The comparison of ET estimates by STEEP, MOD16 and PMLv2 with the observed values at the different sites (Fig. 8) reveals that the ET estimates by STEEP and global products adequately followed the seasonality of the values, with a better fit for STEEP and MOD16. In general, the evaluation at the different sites shows that the *RMSE* of STEEP was not higher than 6.45 mm/8 days, while the ET products' maximum *RMSE* was close to 15 mm/8 days. It is noted that the lowest *RMSE* value found (4.11 mm/8 days) was for MOD16 at the SET site. Regarding R^2 values, 80% of the evaluations with STEEP were equal to or greater than 0.50. For MOD16, 60% of the R^2 values were equal to or greater than 0.70, while for PMLv2, no site had R^2 values that exceeded 0.55. The best *NSE* value produced by STEEP was 0.77, while with MOD16, it was 0.70, both at the SNN site, while PMLv2 did not exceed 0.39 (PTN site). Regarding ρc, the percentages of ET evaluations that obtained values equal to or greater than 0.70 were 60% for STEEP and MOD16, and only 20% for PMLv2 (site PTN). The overestimations (*PBIAS*) with STEEP were not higher than 50%, and not higher than 95% with MOD16. For PMLv2 the overestimations did not exceed 80%, except for the SET site that obtained a *PBIAS* approx. 160%.. We highlight the good performance of MOD16 for the SET, SNN, and especially the PTN sites, with very good performance metrics and seasonal behaviour, capturing ET values in dry periods very well. The evaluation results of STEEP, MOD16 and PMLv2 for all observation sites combined are shown in Fig. 9. Noteworthy is the better performance of STEEP over MOD16 and PMLv2, with *RMSE* of < 6 mm/8 days, R^2 and *NSE* greater than or close to 0.60, ρc of > 0.75 and an average overestimation < 12%. Analysis with the dataset considering only the 8-day time periods without missing field-observed data, i.e. periods with valid ET measurements during eight consecutive days (Fig. S3) did not change the results overall, confirming STEEP's dominance compared to the two standard products evaluated.

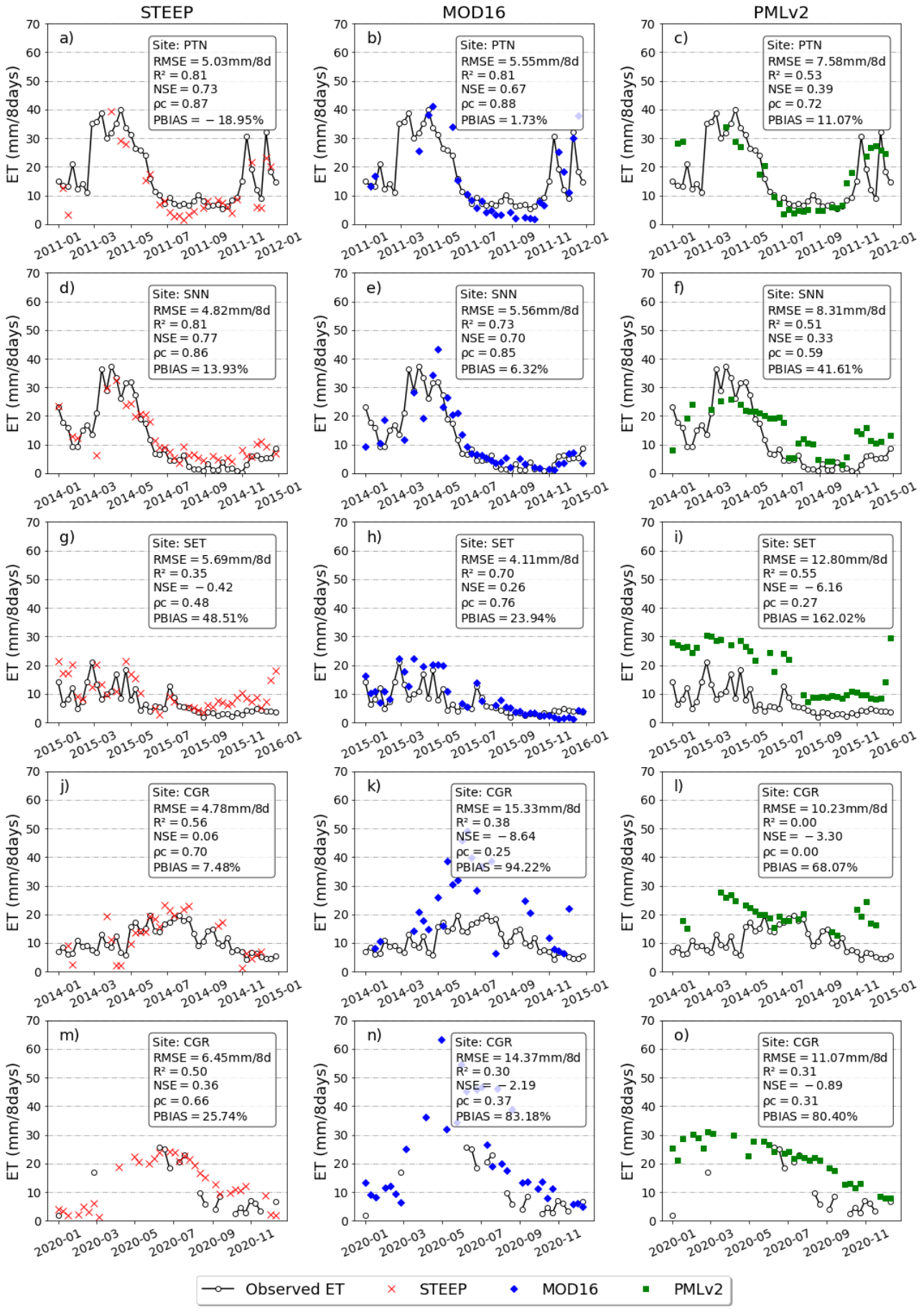
STEEP
MOD16
PMLv2
a)
Site: PTN
RMSE = 5.03mm/8d
R² = 0.81
NSE = 0.73
ρc = 0.87
PBIAS = − 18.95%
b)
Site: PTN
RMSE = 5.55mm/8d
R² = 0.81
NSE = 0.67
ρc = 0.88
PBIAS = 1.73%
c)
Site: PTN
RMSE = 7.58mm/8d
R² = 0.53
NSE = 0.39
ρc = 0.72
PBIAS = 11.07%
d)
Site: SNN
RMSE = 4.82mm/8d
R² = 0.81
NSE = 0.77
ρc = 0.86
PBIAS = 13.93%
e)
Site: SNN
RMSE = 5.56mm/8d
R² = 0.73
NSE = 0.70
ρc = 0.85
PBIAS = 6.32%
f)
Site: SNN
RMSE = 8.31mm/8d
R² = 0.51
NSE = 0.33
ρc = 0.59
PBIAS = 41.61%
g)
Site: SET
RMSE = 5.69mm/8d
R² = 0.35
NSE = − 0.42
ρc = 0.48
PBIAS = 48.51%
h)
Site: SET
RMSE = 4.11mm/8d
R² = 0.70
NSE = 0.26
ρc = 0.76
PBIAS = 23.94%
i)
Site: SET
RMSE = 12.80mm/8d
R² = 0.55
NSE = − 6.16
ρc = 0.27
PBIAS = 162.02%
j)
Site: CGR
RMSE = 4.78mm/8d
R² = 0.56
NSE = 0.06
ρc = 0.70
PBIAS = 7.48%
k)
Site: CGR
RMSE = 15.33mm/8d
R² = 0.38
NSE = − 8.64
ρc = 0.25
PBIAS = 94.22%
l)
Site: CGR
RMSE = 10.23mm/8d
R² = 0.00
NSE = − 3.30
ρc = 0.00
PBIAS = 68.07%
m)
Site: CGR
RMSE = 6.45mm/8d
R² = 0.50
NSE = 0.36
ρc = 0.66
PBIAS = 25.74%
n)
Site: CGR
RMSE = 14.37mm/8d
R² = 0.30
NSE = − 2.19
ρc = 0.37
PBIAS = 83.18%
o)
Site: CGR
RMSE = 11.07mm/8d
R² = 0.31
NSE = − 0.89
ρc = 0.31
PBIAS = 80.40%
ET (mm/8days)
Observed ET
STEEP
MOD16
PMLv2

575

Fig. 8. Temporal evolution of ET from STEEP, MOD16 and PMLv2 for the different observation sites, and their individual performance statistics. a), b) and c) PTN 2011; d), e) and f) SNN 2014; g) h) and i) SET 2015; j), k) and l) CGR 2014; m), n) and o) CGR 2020. Black lines correspond to observed ET while data points refer to estimates by the STEEP model (red crosses), MOD16 (blue diamonds) and PMLv2 (green squares) products.

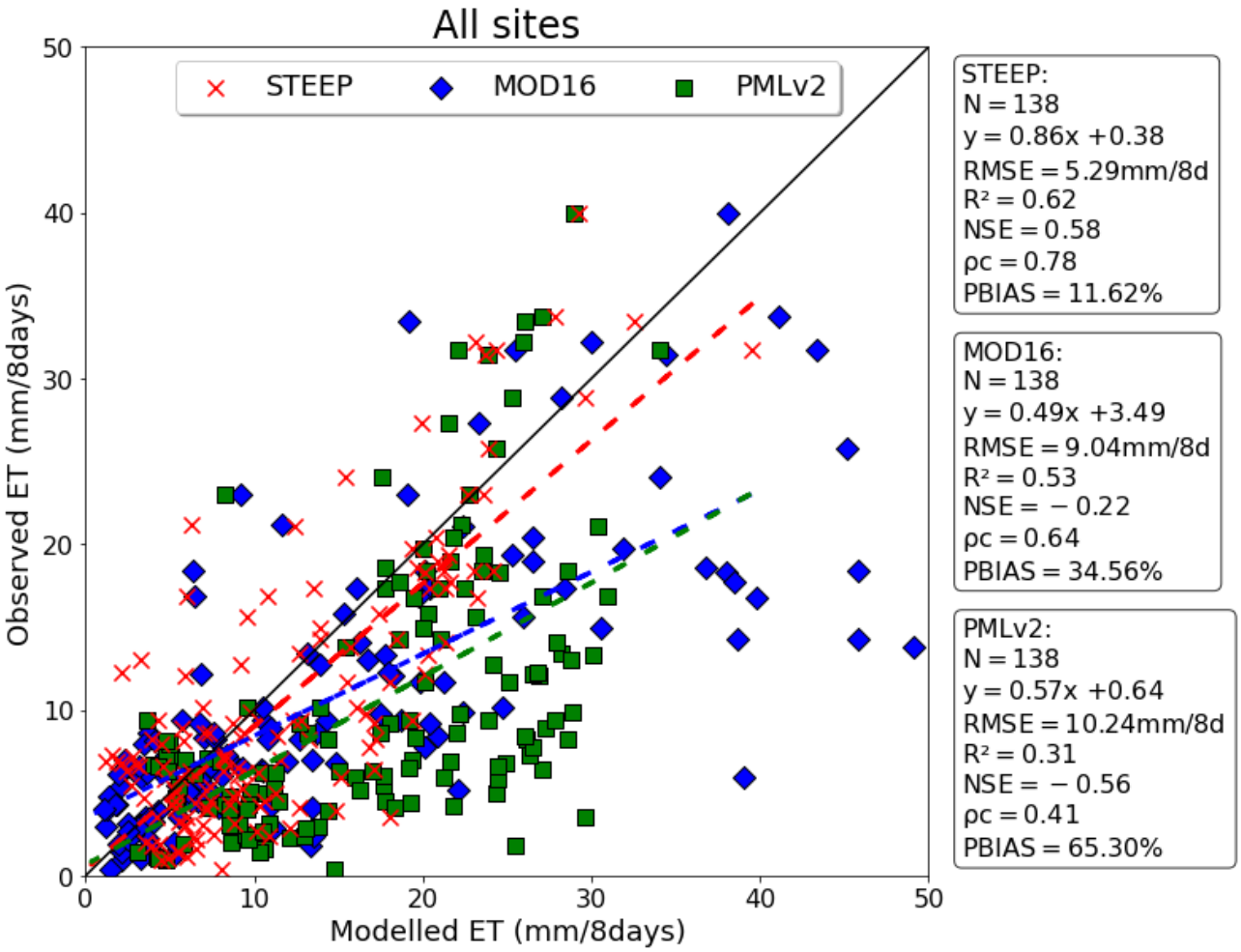

Fig. 9. Evaluation of evapotranspiration (ET, mm/8 days) observed and modelled with STEEP (red crosses), MOD16 (blue diamonds) and PMLv2 (green squares) for all experimental sites. The black line is the 1:1 line; dashed lines are the fitted linear regressions of observed versus modelled values by the STEEP model (red), MOD16 (blue) and PMLv2 (green) products. *N* = 138 is the total number of eight-day periods with at least one day of EC data measured in at least one of the five experimental sites of Caatinga where all the ET models (STEEP, MOD16 and PMLv2) outputs were available.

589 The explanation of the differences between STEEP and the MOD16 and PMLv2 products is
590 two-fold. Firstly, the way ET is obtained differs between STEEP and the other products. While
591 STEEP and other SEB single-source models estimate ET as a combined single process, i.e. soil
592 evaporation and transpiration estimates are provided as a lumped sum (Sahnoun et al., 2021), and
593 interception loss is not taken into account, MOD16 and PMLv2 discriminate the ET components, i.e.
594 soil evaporation, transpiration, and wet canopy evaporation (Mu et al., 2011; Zhang et al., 2019).
595 With this in mind it is remarkable that STEEP performs better than the other, widely used, multiple-
596 source ET products. Secondly, the input data sets and their uses are different. The driving
597 meteorological data for STEEP are from ERA5-Land, while in MOD16, they are from MERRA and in
598 PMLv2 are provided by GLDAS (Mu et al., 2011; Zhang et al., 2019). In addition, the meteorological
599 elements used are different among the ET products. MOD16 requires air temperature, atmospheric
600 pressure, relative humidity, and downward shortwave radiation. In addition to these elements,
601 PMLv2 also requires precipitation, downward longwave radiation, and wind speed (Mu et al., 2011;
602 Zhang et al., 2019; Yin et al., 2020; Chen et al., 2022). Although both ET products use the same
603 land cover data (MOD12Q1), only MOD16 integrates it into its algorithm. In MOD16, the land cover
604 type defines biome delimitation for the characterization of leaf stomatal conductance, vapour
605 pressure deficit (VPD) and other related factors, while PMLv2 only uses land cover to construct a
606 mask of the land area (Chen et al., 2022). The sources and use of LAI in these two products are also
607 different. LAI is used to increase leaf conductance in MOD16, while it is used to divide the total
608 available energy into canopy uptake and soil uptake in PMLv2 (Mu et al., 2011; Zhang et al., 2019;
609 Chen et al., 2022). Although MOD16 uses EC data from 46 distributed sites for validation (Mu et al.,
610 2011) and PMLv2 uses EC data from 95 distributed sites and ten plant functional types for calibration
611 (Zhang et al., 2019; Yin et al., 2020), none of the products had observation sites in SDTF.
612 The uncertainties associated with field measurements of ET can also influence the evaluation
613 of the model products. It is generally accepted that EC flux towers provide reliable local, i.e. for areas
614 of relatively limited spatial extensions, ca. 10 km², ET measurements (Mu et al., 2011; Chu et al.,
615 2021; Salazar-Martínez et al., 2022). However, generally flux tower data have a lack of energy
616 balance closure, that is the difference between net radiation and ground heat flux is sometimes
617 greater than the sum of the turbulent latent and sensible heat fluxes, an error that can be in the of

10–30% range (Wilson et al., 2002; Foken, 2008; Allen et al., 2011). This gap can result from instrument errors, weather and surface conditions, e.g. those that result in advection, and gap-filling methods (Mu et al., 2011). In addition, the complex and heterogeneous canopy structure, the stochastic nature of turbulence (Hollinger and Richardson, 2005) and adverse weather conditions, e.g. rainy and stormy days, tower sensors recording abnormal values, can affect ET measurements obtained by EC systems (Ramoelo et al., 2014).

3.3 Sources of error and further research for STEEP

In its current configuration, STEEP has some limitations that should be noted. Meteorological reanalysis provides only large-scale averages and can misrepresent local meteorological conditions; hence, it suffers from biases, especially over heterogeneous surfaces (Rasp et al., 2018). However, despite moderate accuracy and biases at regional scales, ground-based assimilation and reanalysis data have become important sources of meteorological inputs for ET estimates (Mu et al., 2011; Zhang et al., 2019; Allam et al., 2021; Senay et al., 2022). Laipelt et al. (2020) and Kayser et al. (2022) showed that global reanalysis data when used as meteorological inputs had modest effects only on the accuracy of SEBAL for estimating ET. In our study, ERA5-Land exhibited relatively high and satisfactory agreement with micrometeorological data measured at each site (Fig. S4). Also, although gap-filling was used in the present study to improve the availability of LST data, this procedure should be used with caution. In addition, care should be taken when using the MCD43A4 reflectance product, because in its composition there is also gap-filling. For example, on some cloudy days, the estimates of vegetation indices, surface albedo, and LST may have introduced inaccuracies in the STEEP (and in SEBAL) model calculation process due to these gap-filling methods. Regarding the selection of endmembers pixels, although the temporal evolution of the selected pixels in this study seems plausible, their representativeness of the actual conditions may be debatable, especially considering the considerable extent of the AOI. The computational capacity and the effectiveness of GEE for running SEB models should be commended. Although other studies have demonstrated GEE's strength (Laipelt et al., 2021; Jaafar et al., 2022; Senay et al., 2022), this platform has some limitations when it comes to the number of iterations, e.g. a convergence threshold cannot be set to stop the within-loop iterations of *H* calculations; instead a fixed number of

iterations needs to be defined. Still, the availability of the several necessary datasets within one platform greatly facilitates the run of STEEP and other SEB models.

One of the main focuses of this study is to provide a one-source model capable of representing ET in environments that are mainly governed by soil–water availability, such as those represented by SDTF, in a parsimonious way. Based on our findings we deem this main aim to be achieved due to the relative simplicity of the STEEP model and its low data demand. The improved performance of STEEP was the result of improvement of existing and physically meaningful parameters (*z0m* and kB^{-1}), rather than by introducing additional empirical parameters, thereby satisfying the principle of equifinality (see Beven and Freer, 2001). To explore further the potential and accuracy of STEEP, more research is needed to analyse the impact that the improved *H* approach has on ET of different land covers at longer time scales. Despite the promising overall results, additional efforts are required on modelling *H* in SDTF regions. Although we have shown that STEEP outperforms other models in simulating either *H* or ET, we acknowledge that there is still room for model improvement. Given that the STEEP model was formulated to be a calibration-free model, it may be possible to improve *H* estimates by, for example, optimising coefficients associated to soil moisture (see Eq A.12) and applying dynamic values to αpt (see Eq A.25) varying seasonally. Another potential improvement for instantaneous H estimates can be achieved by accounting for biomass heat storage (BHS; Swenson et al., 2019) in STEEP. Meier et al. (2019) have shown that considering BHS can enable land surface models to capture the diurnal asymmetry of the temperature impact on energy fluxes and, consequently, provide improved sub-hourly *H*. Improving the quantification of regional ET via RS-based SEB models has a great potential to provide a more accurate estimate of the energy and water fluxes in SDTF regions, and will contribute to a better understanding of the water cycle, its uses, and the interrelationships with ecosystem functioning.

4. Conclusions

Our work developed a calibration-free model (STEEP) with an improved approach for estimating the latent and sensible heat fluxes by remote sensing for SDTF. In summary, the main conclusions are:

- The estimates of *H* by STEEP allowed ET estimates to be closer to the observed field values than those obtained by SEBAL. Based on all the performance metrics used to

analyse the models, STEEP was superior to SEBAL. STEEP showed *RMSE* less than 1mm/day, R^2 between 0.24 and 0.69, *NSE* between -0.17 and 0.65, ρc between 0.41 and 0.80 and *PBIAS* between -17% to 54%. Also noteworthy is how well STEEP captured the seasonal course of observed ET.

- Compared with ET data from the global MOD16 and PMLv2 products, the STEEP model simulated a similar but generally superior seasonal evolution and its performance metrics were also better. Considering all observation sites simultaneously, at the eight-day scale, STEEP showed superior performance with *RMSE* less than 6 mm/8 days, R^2 and *NSE* equal to or greater than 0.60, ρc greater than 0.75, and an overestimation of < 12%.

Thus, we conclude that STEEP, a one-source model that incorporated the seasonality of the aerodynamic and surface variables, was well-heeled in representing ET in environments that are mainly governed by soil–water availability. All the same, there is a need to evaluate the newly developed STEEP model performance for different land covers, climate, and for longer time series than those considered during the modelling process in this study.

Acknowledgements

The Coordenação de Aperfeiçoamento de Pessoal de Nível Superior-Brazil (CAPES)-Finance Code 001, provided scholarships to the first and fifth authors. This work was funded by the Brazilian National Council for Scientific and Technological Development (CNPq), grant 409341/2021-5, by the Paraiba Scientific Foundation (FAPESQ), under grants 010/2021 and 403/2021, and by São Paulo Scientific Foundation (FAPESP), grant 2015/24461-2. CEF is a research unit funded by Fundação para a Ciência e a Tecnologia I.P. (FCT), Portugal (UIDB/00239/2020). MSBM, AV and RLBN acknowledge support by the Newton/NERC/FAPESP Nordeste project (NE/N012526/1 ICL 652 and NE/N012488/1 UoR). RLBN acknowledges support from the European Research Council under the European Union's Horizon 2020 research and innovation programme (grant agreement No: 787203 REALM). MSBM thanks to Fundação de Amparo à Ciência e Tecnologia do Estado de Pernambuco (FACEPE) for funding this through the Project FACEPE APQ 0062-1.07/15 (Caatinga-FLUX). MSBM and AMPM acknowledge to the National Observatory of Water and Carbon Dynamics in the Caatinga Biome (INCT: NOWCBCB) supported by FACEPE (grant: APQ-0498-3.07/17 ONDACBC), CNPq (grant: 465764/2014-2), and CAPES (grants: 88887.136369/2017-00).

Data Availability Statement

ET data for the PTN, SNN, and SET sites were published by Melo et al. (2021), and are available at https://doi.org/10.5281/zenodo.5549321. ET data for the CGR site; H data for the PTN, SNN, CGR sites, and the code used for the formulation of the STEEP model presented in this study can be accessed at https://doi.org/10.5281/zenodo.7109043 and https://github.com/ulissesaalencar/ET_SDTF, respectively. H data for the SET site is publicly available for download at https://ameriflux.lbl.gov/.

Supplementary material

Table S1. Performance statistics by the exclusion/modification of one or two parameters/variables implemented in the STEEP model, in the wet and dry seasons: scale factor soil moisture correction (SF), the parameter kB^{-1}, the aerodynamic resistance for heat transfer (rah), PAI replace with LAI (determined by two different methods), the roughness length for momentum transport ($z0m$), the residual latent heat flux in the end members pixels ($r\lambda ET$), and of the SEBAL model.

717

Site		Performance statistics									
		RMSE		*R^2*		*NSE*		*ρ_c*		*PBIAS*	
		wet	*dry*	*wet*	*dry*	*wet*	*dry*	*wet*	*dry*	*wet*	*dry*
PTN (N = 239; 2011)	STEEP	1.23	0.7	0.53	0.62	0.34	0.5	0.68	0.77	-18.01	-17.01
	(-) SF	1.38	0.69	0.56	0.58	0.16	0.52	0.65	0.75	-26.39	-7.99
	(-) kB-1	1.39	0.67	0.54	0.62	0.14	0.55	0.66	0.78	-23.37	-8.23
	(-) rah	1.61	0.66	0.42	0.6	-0.22	0.55	0.54	0.77	-32.42	-6.56
	*LAI**	1.37	1.08	0.57	0.59	0.19	-0.18	0.68	0.59	-24.24	-56.26
	*LAI***	1.27	0.91	0.54	0.34	0.28	0.17	0.68	0.57	-19.73	-11.95
	(-) z0m	1.48	0.88	0.36	0.3	0.01	0.21	0.5	0.54	-25.94	7.55
	(-) rλET	1.5	1.6	0.12	0.19	-0.15	-1.54	0.31	0.28	14.75	75.96
	(-) z0m & rah	1.51	0.72	0.44	0.51	-0.04	0.48	0.57	0.7	-28.85	4.4
	(-)rah & rλET	1.47	1.66	0.13	0.15	-0.11	-1.81	0.33	0.23	12.99	81.63
	(-) z0m & rλET	1.42	1.45	0.14	0.09	-0.31	-0.04	0.36	0.22	0.73	57.29
	SEBAL	1.39	1.55	0.16	0.12	0.01	-1.43	0.38	0.23	2.12	69.2
SNN (N = 267; 2014)	STEEP	1.03	0.6	0.46	0.62	0.32	0.25	0.64	0.68	-12.17	58.08
	(-) SF	1.07	0.58	0.47	0.64	0.29	0.44	0.6	0.73	-17.2	42.77
	(-) kB-1	1.12	0.67	0.44	0.59	0.21	0.24	0.6	0.69	-17.86	50.26
	(-) rah	1.19	0.6	0.49	0.62	0.19	0.41	0.57	0.7	-25.47	47.33
	*LAI**	1.38	0.8	0.54	0.3	-0.21	-0.07	0.6	0.44	-29.33	-58.36
	*LAI***	1.19	0.98	0.52	0.09	0.07	-0.6	0.62	0.26	23.77	55.02
	(-) z0m	1.14	0.83	0.41	0.23	0.24	-0.16	0.5	0.37	-19.01	60.45
	(-) rλET	1.16	1.18	0.32	0.43	0.18	-1.33	0.51	0.41	12.96	122.85
	(-) z0m & rah	1.19	0.63	0.52	0.57	0.17	0.34	0.52	0.64	-26.49	50.69
	(-)rah & rλET	1.13	1.14	0.25	0.37	0.16	-1.19	0.47	0.41	6.43	111.65
	(-) z0m & rλET	1.13	1.03	0.24	0.17	0.16	-0.79	0.47	0.32	-5.86	79.17
	SEBAL	1.13	1.06	0.22	0.33	0.16	-0.88	0.45	0.41	0.91	98.12
SET (N = 283; 2015)	STEEP	1.16	0.6	0.12	0.12	-0.55	-0.94	0.28	0.27	52.19	55.18

	(-) SF	1.04	0.61	0.11	0.02	-0.25	-0.99	0.28	0.14	36.58	38.26
	(-) kB-1	1.13	0.58	0.06	0.07	-0.49	-0.86	0.21	0.23	36.71	40.83
	(-) rah	1.06	0.56	0.04	0	-0.43	-1.03	0.18	0.03	21.82	39.71
	*LAI**	1.3	0.68	0.03	0.09	-0.98	-1.51	0.12	0.2	-62.3	-75.32
	*LAI***	1.15	0.6	0.04	0.05	-0.53	-0.97	0.19	0.21	-6.83	-29.78
	(-) z0m	1.09	0.75	0.1	0	-0.36	-2.74	0.26	-0.02	42.62	80.96
	(-) rλET	2.11	1.37	0.15	0.04	-4.18	-9.27	0.15	0.06	151.66	190.07
	(-) z0m & rah	1.06	0.58	0.05	0	-0.3	-1.24	0.21	0.02	21.6	51.96
	(-)rah & rλET	1.99	1.37	0.11	0.01	-3.99	-9.27	0.13	0.04	143.27	183.22
	(-) z0m & rλET	1.66	1.16	0.07	0.01	-2.47	-6.31	0.14	0.04	104.32	134.34
	SEBAL	1.83	1.28	0.1	0	-3.21	-7.93	0.14	0.03	128	161.89
CGR (N = 171; 2014)	STEEP	0.8	0.72	0.35	0.51	-0.35	-0.8	0.55	0.58	5.85	25.16
	(-) SF	0.7	0.67	0.36	0.52	-0.02	-0.53	0.59	0.6	6.57	30.14
	(-) kB-1	0.78	0.8	0.25	0.44	-0.28	-1.18	0.47	0.51	15.04	38.9
	(-) rah	0.71	0.78	0.28	0.46	-0.06	-1.07	0.51	0.48	-8.54	54.63
	*LAI**	0.76	0.83	0.49	0.61	-0.23	-1.35	0.64	0.51	-7.64	-62.39
	*LAI***	0.75	0.68	0.46	0.58	-0.18	-0.57	0.63	0.63	-9.25	-26.31
	(-) z0m	0.71	0.83	0.28	0.35	-0.05	-1.35	0.51	0.38	-11.12	62.72
	(-) rλET	1.15	2.32	0.09	0.07	-1.77	-17.48	0.19	0.04	46.68	217.84
	(-) z0m & rah	0.69	0.84	0.24	0.44	-0.01	-1.43	0.48	0.39	3.9	68.9
	(-)rah & rλET	1.14	2.44	0.05	0.03	-1.72	-19.4	0.15	0.02	43.77	229.58
	(-) z0m & rλET	0.85	1.97	0.11	0.04	-0.51	-12.27	0.33	0.04	9.18	175.39
	SEBAL	0.97	2.24	0.07	0.03	-0.97	-14.7	0.21	0.03	28.63	208.13
CGR (N = 48; 2020)	STEEP	0.61	1.06	0.39	0.02	0.29	-2.98	0.62	0.09	-1.19	101.37
	(-) SF	0.82	1.03	0.3	0	-0.29	-2.76	0.52	0.02	-6.52	106.36
	(-) kB-1	0.83	1.26	0.29	0	-0.3	-4.63	0.51	-0.03	-5.31	135.98
	(-) rah	1.11	1.13	0.25	0	-1.2	-3.55	0.42	-0.02	-15.37	133.29
	*LAI**	0.85	1.02	0.29	0.01	-0.38	-0.99	-3.06	0.4	-4.71	31.63
	*LAI***	0.67	0.76	0.36	0.07	0.14	-1.03	0.59	0.26	-3.58	2.87

(-) z0m	0.69	1.03	0.41	0	0.15	-2.73	0.58	-0.02	-12.29	106.1
(-) rλET	0.99	2.25	0.03	0.06	-0.52	-16.98	0.17	-0.04	6.37	312.54
(-) z0m & rah	1.04	1.13	0.34	0.01	-0.74	-3.52	0.5	-0.03	-16.56	134.92
(-)rah & rλET	0.89	2.38	0.05	0.14	-0.24	-19.08	0.22	-0.05	1.07	330.94
(-) z0m & rλET	0.83	1.77	0.18	0.02	-0.6	-10.14	0.33	-0.04	-14.15	216.81
SEBAL	0.81	2.11	0.16	0.07	-0.02	-0.02	0.31	-0.04	-12.25	285.53

718

719 *z0m* = roughness length for momentum transfer; *rah* = aerodynamic resistance for heat transfer; r*λET* = remaining *λET* in the endmembers pixels.

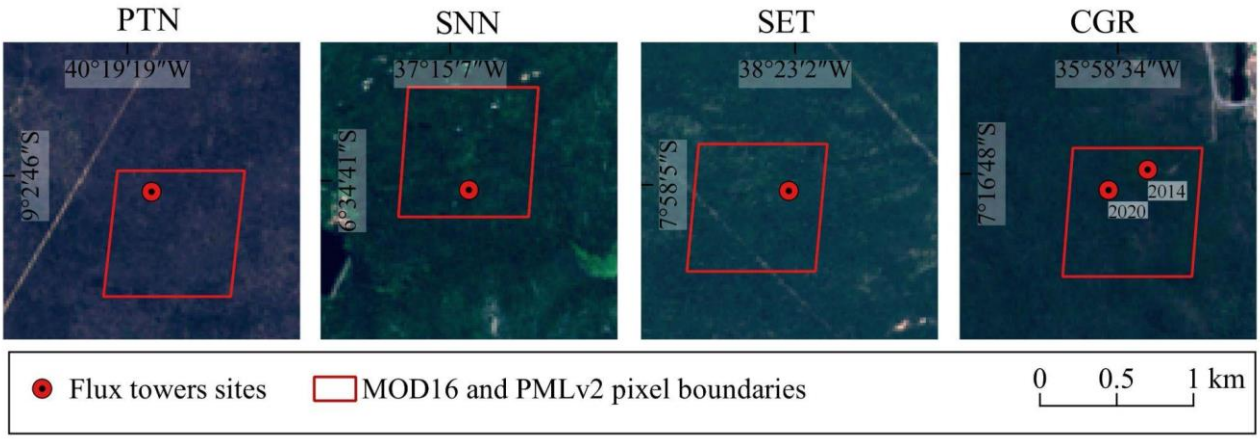

720

721 Fig. S1. Location of the flux towers sites and MOD16 and PMLv2 pixel boundaries. True colour
722 composite (bands 4, 3, and 2) of Harmonized Sentinel-2 MSI acquired via Google Earth Engine.
723 Scene acquired of PTN (12/06/2021); SNN and SET (25/05/2021); CGR (29/07/2021).

724

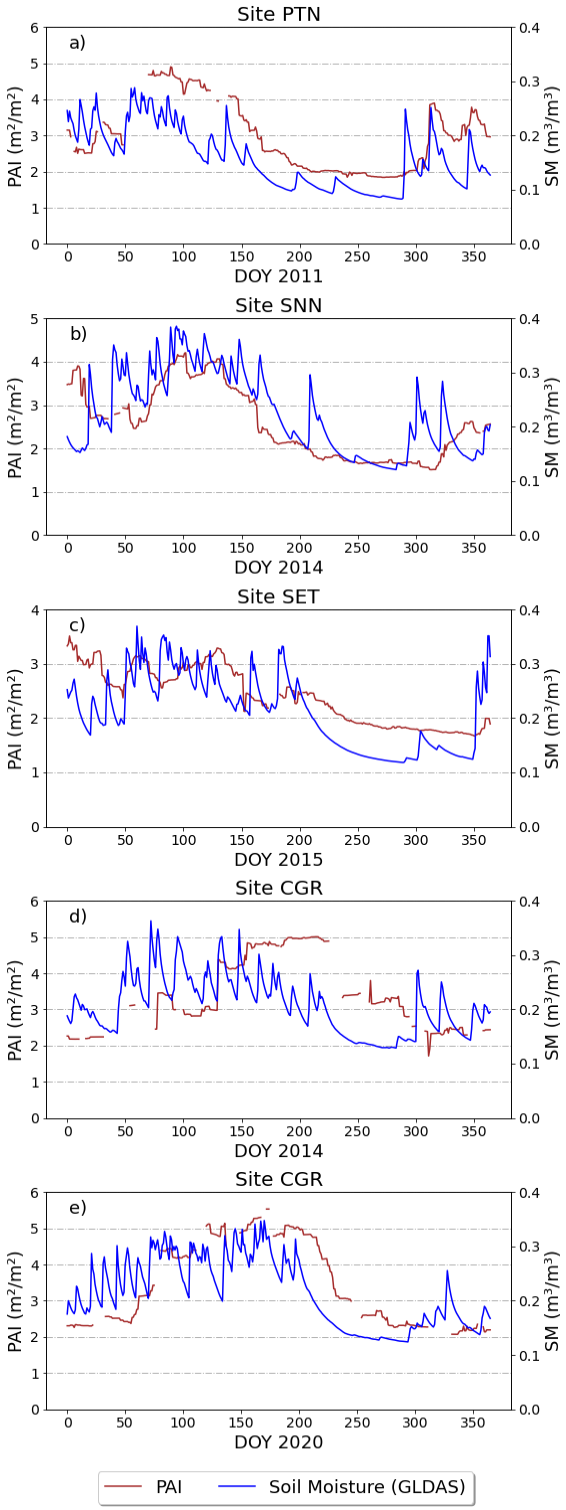

Fig. S2. PAI and soil moisture time series for the different observation sites.

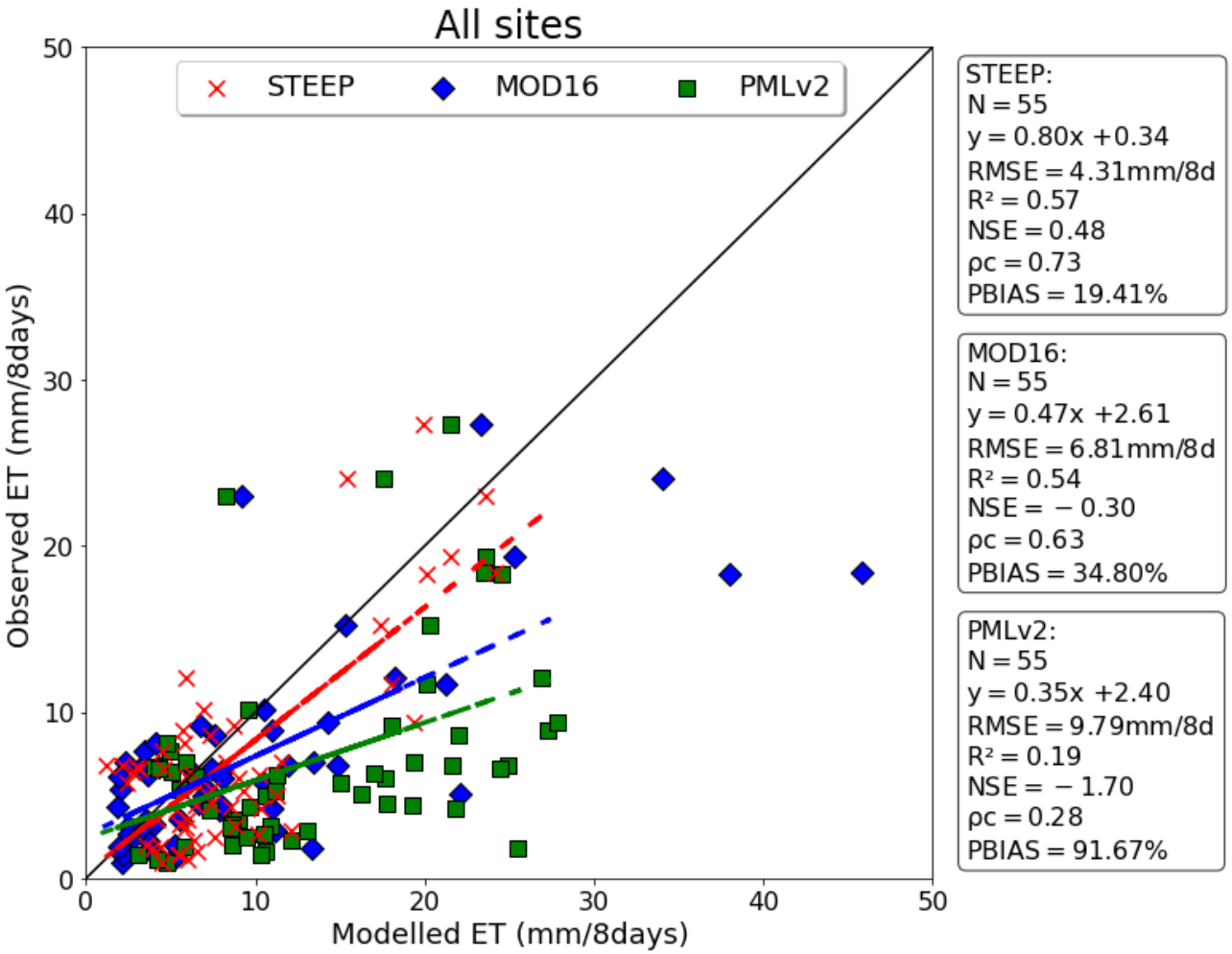

Fig. S3. Evaluation of evapotranspiration (ET, mm/8 days) observed and modelled with STEEP (red crosses), MOD16 (blue diamonds) and PMLv2 (green squares) for all experimental sites considering only the 55 periods where the field-observed data had eight consecutive days. The black line is the 1:1 line; dashed lines are the fitted linear regressions of observed or modelled values by the STEEP model (red), MOD16 (blue) and PMLv2 (green) products.

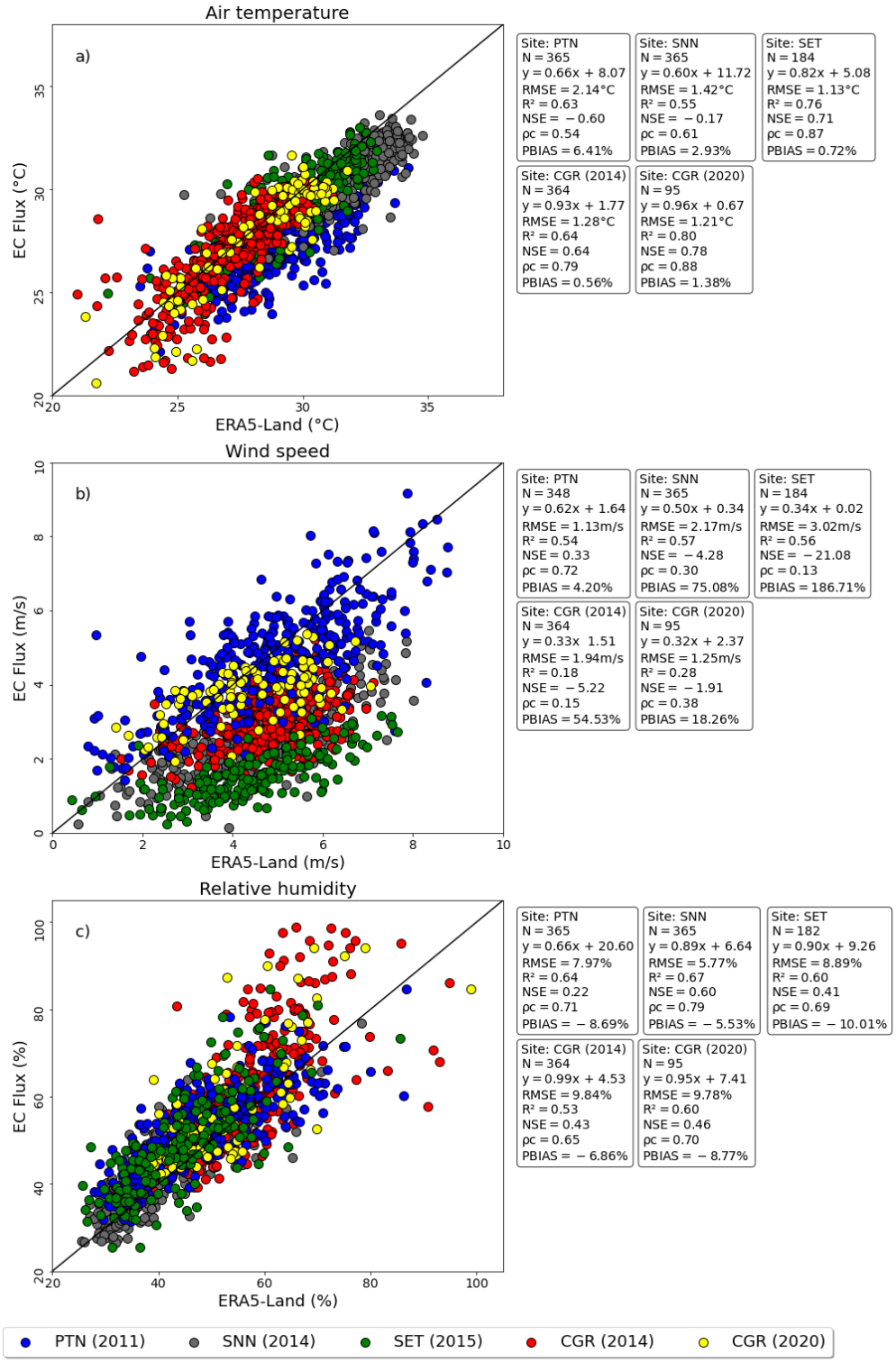

Fig. S4. Comparison between ERA5-Land reanalysis dataset and local observational meteorological measurements from the flux tower at the closest time from the satellite overpass. Micrometeorological sensors installed at the flux towers are up to 16 m in distance from the land surface, and ERA5-Land variables have different reference elevation (e.g. 2 m for air temperature and 10 m to wind speed).

Appendix A – Equations adopted to formulate the STEEP model

Latent heat flux (λET) was modeled using Eq. (A.1):

$$\lambda ET = Rn - G - H \quad \text{(A.1)}$$

where R_n is net radiation, G is soil heat flux, and H is sensible heat flux. All variables are expressed in energy units (e.g., W/m^2).

Net radiation (Rn) was modeled based on the radiation budget indicated by Allen et al. (2007) and Ferreira et al. (2020) by Eq. (A.2):

$$Rn = R_{S\downarrow} \times (1 - \alpha) + \varepsilon_S \times R_{L\downarrow} - R_{L\uparrow} \quad \text{(A.2)}$$

where $R_{S\downarrow}$ is incident shortwave radiation (W/m^2) estimated following Allen et al. (2007), α is surface albedo (dimensionless), estimated following Trezza et al. (2013), $R_{L\downarrow}$ is longwave radiation from the atmosphere (W/m^2) estimated following Ferreira et al. (2020) with atmospheric emissivity from Duarte et al. (2006); $R_{L\uparrow}$ is emitted longwave radiation (W/m^2) following Ferreira et al. (2020) with ε_S the surface emissivity (dimensionless), estimated following Long et al. (2010).

Soil heat flux (G), expressed as a ratio of net radiation, was estimated following the model by Bastiaanssen et al. (1998):

$$\frac{G}{Rn} = [(LST - 273.15) \times (0.0038 + 0.0074 \times \alpha) \times (1 - 0.98 \times NDVI^4)] \quad \text{(A.3)}$$

where *LST* is the surface temperature (K) and NDVI is the Normalized Difference Vegetation Index (dimensionless), estimated following Rouse et al. (1973).

Sensible heat flux (H) was modeled using:

$$H = \frac{\rho \times c_p \times dT}{rah} \quad \text{(A.4)}$$

where ρ is the air density (kg/m^3), c_p refers to the specific heat of air at constant pressure (J/kg/K), *dT* is the temperature gradient (K), and *rah* is the aerodynamic resistance for heat transfer (s/m).

Aerodynamic resistance to heat transport was estimated based on the classical equation given in Paul et al. (2013), see also Verhoef et al. (1997a):

$$rah = \frac{1}{k \times u^*} \times \left[ln \left(\frac{z_{ref} - d0}{z0m} \right) - \psi_h \right] + \frac{1}{k \times u^*} \times kB_{umd}^{-1} \quad \text{(A.5)}$$

where k is the von Kármán constant taken as 0.41, u^* is the friction velocity (m/s), z_{ref} is the reference height (m), *d0* is zero plane displacement height (m), *z0m* is roughness length for momentum transfer (m), ψ_h is the atmospheric stability correction function for heat transfer (m), as calculated following Paulson (1970), kB_{umd}^{-1} is the dimensionless parameter formulated to express the excess resistance of heat transfer compared to momentum transfer, corrected for soil moisture derived from remote sensing.

The friction velocity was computed according to Verhoef et al. (1997b) and Paul et al. (2013):

$$u^* = k \times u \left[ln \left(\frac{z_{ref} - d0}{z0m} \right) - \psi_m \right]^{-1} \quad \text{(A.6)}$$

where u is the wind speed (m/s) at a known height z_{ref}, ψ_m is the atmospheric stability correction function for momentum transfer (m), as calculated following Paulson (1970).

Roughness length for momentum transport was estimated, based on the studies by Verhoef et al. (1997b):

$$z0m = (HGHT - d0) \times exp^{(-k \times \gamma + PSICORR)} \quad \text{(A.7)}$$

where $HGHT$ is the height of the vegetation (m), $PSICORR$ is taken as 0.2 and γ is the inverse of the square root of the bulk surface drag coefficient at the roughness canopy height (Raupach, 1992).

Zero plane displacement height ($d0$) was obtained following Raupach (1994) from:

$$d0 = HGHT \times \left[\left(1 - \frac{1}{\sqrt{CD1 \times PAI}} \right) + \left(\frac{exp^{-\sqrt{CD1 \times PAI}}}{\sqrt{CD1 \times PAI}} \right) \right] \quad \text{(A.8)}$$

where $CD1$ is taken as 20.6 and *PAI* is the Plant Area Index.

γ was following Verhoef et al. (1997b):

$$\gamma = \left(CD + CR \times \frac{PAI}{2} \right)^{-0.5} \quad \text{(A.9)}$$

if γ < 3.33, γ is set to 3.33. Following Verhoef et al. (1997), CD and CR are taken as 0.01 and 0.35, respectively.

Plant Area Index was calculated according to Miranda et al. (2020) as:

$$PAI = 10.1 \times \left(\rho_{NIR} - \sqrt{\rho_{RED}} \right) + 3.1 \quad \text{(A.10)}$$

where ρ_{NIR} is the near infrared band reflectance, and ρ_{RED} is the red band reflectance. If *PAI* < 0, *d0* is set to 0.

The dimensionless parameter kB_{umd}^{-1} is corrected by soil moisture by remote sensing following the equations provided by Gokmen et al. (2012):

$$kB_{umd}^{-1} = SF \times kB^{-1} \quad \text{(A.11)}$$

where *SF* is a scaling factor, represented by a sigmoid function:

$$SF = \left[c + \frac{1}{1 + exp^{(d - e \times SM_{rel})}}\right] \quad \text{(A.12)}$$

Here, c, d, e are the sigmoid function coefficients, for which we adopted values of 0.3, 2.5, and 4, respectively, following Gokmen et al. (2012). SM_{rel} is the relative soil moisture, obtained from:

$$SM_{rel} = \frac{SM - SM_{min}}{SM_{max} - SM_{min}} \quad \text{(A.13)}$$

where SM is the actual soil moisture content, in our case obtained with the GLDAS reanalysis product, and SM_{min} and SM_{max} are the minimum and maximum soil moisture. The SM_{min} and SM_{max} values were obtained using the annual time series analysis of the soil moisture data.

kB^{-1} was calculated according to Su et al. (2001):

$$kB^{-1} = \frac{k \times Cd}{4 \times Ct \times \frac{u^*}{u(h)} \times \left(1 - exp^{\left(-\frac{nec}{2}\right)}\right)} \times f_c^2 + \frac{k \times \frac{u^*}{u(h)} \times \frac{z0m}{h}}{C_t^*} \times f_c^2 \times f_s^2 + kBs^{-1} \times f_s^2 \quad \text{(A.14)}$$

where $kBs^{-1} = 2.46(Re^*)^{0.25} - 2$, Cd is the drag coefficient of the foliage elements taken as 0.2, Ct is the heat transfer coefficient of the leaf with value 0.01.

The ratio $\frac{u^*}{u(h)}$ is parameterized as:

$$\frac{u^*}{u(h)} = c1 - c2 \times exp^{(-c3 \times Cd \times PAI)} \quad \text{(A.15)}$$

where $c1$ = 0.320, $c2$ = 0.264, $c3$ = 15.1.

nec is the extinction coefficient of the wind speed profile within the canopy given by:

$$nec = \frac{Cd \times PAI}{\frac{2u^{*2}}{u(h)^2}} \quad \text{(A.16)}$$

797 C_t^* is heat transfer coefficient of the soil given by:

$$C_t^* = Pr^{-2/3} \times (Re)^{-1/2} \quad \text{(A.17)}$$

798 where Pr is the Prandtl number with a value 0.71, and Re is the Reynolds number calculated as:

$$Re = \frac{u^* \times 0.009}{v}, \qquad v = 1.461 \times 10^{-5} \quad \text{(A.18)}$$

799 where v is the kinematic viscosity (m^2/s).

800 In Eq. A.14 f_c is the fractional canopy cover calculated according to Eq. (A19), and f_s is its
801 complement.

$$f_c = 1 - \left[\frac{NDVI - NDVI_{max}}{NDVI_{min} - NDVI_{max}}\right]^{0.4631} \quad \text{(A.19)}$$

802 where $NDVI_{max}$ and $NDVI_{min}$ are maximum and minimum NDVI values, respectively. $NDVI_{max}$ and
803 $NDVI_{min}$ values were obtained using the annual time series analysis of the NDVI.

804 *dT* in Eq. (A4) was estimated daily with a linear relationship on the surface temperature
805 (Bastiaanssen et al., 1998) as:

$$dT = a + b \times LST \quad \text{(A.20)}$$

806 To find the coefficients a and b in Eq. (A20) requires that hot and cold endmembers pixels are
807 established. The coefficients were found as:

$$b = \frac{(dT_{hot} - dT_{cold})}{(LST_{hot} - LST_{cold})} \quad \text{(A.21)}$$

$$a = dT_{cold} - b \times LST_{cold} \quad \text{(A.22)}$$

$$dT_{hot/cold} = \frac{H_{hot/cold} \times rah_{hot/cold}}{\rho \times c_p} \quad \text{(A.23)}$$

$$H_{hot/cold} = Rn_{hot/cold} - G_{hot/cold} - \lambda ET_{hot/cold} \quad \text{(A.24)}$$

where $dT_{hot/cold}$ are dT values for the hot/dry and cold/wet endmember pixels, respectively, $Rn_{hot/cold}$, $G_{hot/cold}$, $LST_{hot/cold}$, $rah_{hot/cold}$ are the median values extracted on the endmember pixels of each variable. The selection of endmember pixels is detailed in section 2.3.

$\lambda ET_{hot/cold}$ is the term incorporated in the computation of *H* in the endmember pixels given by the Priestley-Taylor (1972) equation, according to Singh and Irmak (2011) and French et al. (2015):

$$\lambda ET_{hot/cold} = \left(Rn_{hot/cold} - G_{hot/cold}\right) \times f_c \times \alpha pt \times \left[\frac{\Delta}{\Delta + \gamma_c}\right] \quad \text{(A.25)}$$

where αpt is the empirical Priestley-Taylor coefficient, nominally set to 1.26, but here adjusted according to local conditions, i.e. we adopted the αpt values (0.55 for hot/dry and 1.75 for cold/wet pixels) based on Ai and Yang (2016). Δ is the slope of the saturation vapor pressure-air temperature curve (kPa/ºC) and γ_c is the psychrometric constant (kPa/ºC).

The actual daily evapotranspiration (mm/day) was obtained by means of the following relationship:

$$ET_{24h} = \frac{86400}{(2.501 - 0.00236 \times T_a) \times 10^6} \times \frac{\lambda ET}{Rn - G} \times Rn_{24h} \quad \text{(A.26)}$$

where T_a is the mean daily air temperature (°C), *λET* is derived from Eq. A1, and Rn_{24h} corresponds to the daily net radiation (W/m^2); in this study both driving variables were obtained with data from the ERA5-Land product.

References

Ai, Z., & Yang, Y. (2016). Modification and Validation of Priestley–Taylor Model for Estimating Cotton Evapotranspiration under Plastic Mulch Condition. Journal of Hydrometeorology, 17(4), 1281–1293. doi:10.1175/jhm-d-15-0151.1

Akoglu, H. (2018). User's guide to correlation coefficients. Turkish Journal of Emergency Medicine, 18(3), 91-93. doi: 10.1016/j.tjem.2018.08.001

Alberton, B., Torres, R. da S., Cancian, L. F., Borges, B. D., Almeida, J., Mariano, G. C., … Morellato, L. P. C. (2017). Introducing digital cameras to monitor plant phenology in the tropics: applications for conservation. Perspectives in Ecology and Conservation, 15(2), 82–90. doi:10.1016/j.pecon.2017.06.004

831 Allam, M., Mhawej, M., Meng, Q., Faour, G., Abunnasr, Y., Fadel, A., & Xinli, H. (2021). Monthly 10-
832 m evapotranspiration rates retrieved by SEBALI with Sentinel-2 and MODIS LST data. Agricultural
833 Water Management, 243, 106432. doi:10.1016/j.agwat.2020.106432

834 Allen, R. G., Tasumi, M., & Trezza, R. (2007). Satellite-Based Energy Balance for Mapping
835 Evapotranspiration with Internalized Calibration (METRIC)—Model. Journal of Irrigation and
836 Drainage Engineering, 133(4), 380–394. doi:10.1061/(asce)0733-9437(2007)133:4(380)

837 Allen, K., Dupuy, J. M., Gei, M. G., Hulshof, C., Medvigy, D., Pizano, C., … Powers, J. S. (2017).
838 Will seasonally dry tropical forests be sensitive or resistant to future changes in rainfall regimes?
839 Environmental Research Letters, 12(2), 023001. doi:10.1088/1748-9326/aa5968

840 Allen, R. G., Pereira, L. S., Howell, T. A., & Jensen, M. E. (2011). Evapotranspiration information
841 reporting: I. Factors governing measurement accuracy. Agricultural Water Management, 98(6), 899–
842 920. doi:10.1016/j.agwat.2010.12.015

843 Alvares, C. A., Stape, J. L., Sentelhas, P. C., Gonçalves, J. D. M., & Sparovek, G. (2013). Köppen's
844 climate classification map for Brazil. Meteorologische Zeitschrift, 22(6), 711-728. doi:10.1127/0941-
845 2948/2013/0507

846 Anapalli, S. S., Ahuja, L. R., Gowda, P. H., Ma, L., Marek, G., Evett, S. R., & Howell, T. A. (2016).
847 Simulation of crop evapotranspiration and crop coefficients with data in weighing lysimeters.
848 Agricultural Water Management, 177, 274–283. doi:10.1016/j.agwat.2016.08.009

849 Anderson, M. C., Kustas, W. P., Norman, J. M., Hain, C. R., Mecikalski, J. R., Schultz, L., … Gao,
850 F. (2011). Mapping daily evapotranspiration at field to continental scales using geostationary and
851 polar orbiting satellite imagery. Hydrology and Earth System Sciences, 15(1), 223–239.
852 doi:10.5194/hess-15-223-2011

853 Andrade, J., Cunha, J., Silva, J., Rufino, I., & Galvão, C. (2021). Evaluating single and multi-date
854 Landsat classifications of land-cover in a seasonally dry tropical forest. Remote Sensing
855 Applications: Society and Environment, 22, 100515. doi:10.1016/j.rsase.2021.100515

856 Antonino, A. C. D. (2019), AmeriFlux BASE BR-CST Caatinga Serra Talhada, Ver. 1-5, AmeriFlux
857 AMP, (Dataset). https://doi.org/10.17190/AMF/1562386

858 Araújo, J. C., & González Piedra, J. I. (2009). Comparative hydrology: analysis of a semiarid and a
859 humid tropical watershed. Hydrological Processes, 23(8), 1169–1178. doi:10.1002/hyp.7232

860 Barbosa, H. A., Huete, A. R., & Baethgen, W. E. (2006). A 20-year study of NDVI variability over the
861 Northeast Region of Brazil. Journal of Arid Environments, 67(2), 288–307.
862 doi:10.1016/j.jaridenv.2006.02.022

863 Barbosa, A. D. S., Andrade, A. P. de, Félix, L. P., Aquino, Í. D. S., & Silva, J. H. C. S. (2020).
864 Composição, similaridade e estrutura do componente arbustivo-arbóreo de áreas de Caatinga.
865 Nativa, 8(3), 314–322. doi:10.31413/nativa.v8i3.9494

866 Barraza, V., Restrepo-Coupe, N., Huete, A., Grings, F., Beringer, J., Cleverly, J., & Eamus, D.
867 (2017). Estimation of latent heat flux over savannah vegetation across the North Australian Tropical
868 Transect from multiple sensors and global meteorological data. Agricultural and Forest Meteorology,
869 232, 689-703. doi:10.1016/j.agrformet.2016.10.013

870 Bastiaanssen, W. G. M. (1995). Regionalization of surface flux densities and moisture indicators in
871 composite terrain: A remote sensing approach under clear skies in Mediterranean climates.
872 Wageningen University and Research.

873 Bastiaanssen, W. G. M., Menenti, M., Feddes, R. A., & Holtslag, A. A. M. (1998). A remote sensing
874 surface energy balance algorithm for land (SEBAL). 1. Formulation. Journal of Hydrology, 212-213,
875 198–212. doi:10.1016/s0022-1694(98)00253-4

876 Bastiaanssen, W. G. M., Ahmad, M.-D., & Chemin, Y. (2002). Satellite surveillance of evaporative
877 depletion across the Indus Basin. Water Resources Research, 38(12), 9–1–9–9.
878 doi:10.1029/2001wr000386

879 Bastiaanssen, W. G. M., Noordman, E. J. M., Pelgrum, H., Davids, G., Thoreson, B. P., & Allen, R.
880 G. (2005). SEBAL Model with remotely sensed data to improve water-resources management under

881 actual field conditions. Journal of Irrigation and Drainage Engineering, 131(1), 85–93.
882 doi:10.1061/(asce)0733-9437(2005)131:1(85)

883 Beven, K., & Freer, J. (2001). Equifinality, data assimilation, and uncertainty estimation in
884 mechanistic modelling of complex environmental systems using the GLUE methodology. Journal of
885 Hydrology, 249(1–4), 11–29. doi:10.1016/s0022-1694(01)00421-8

886 Bhattarai, N., Quackenbush, L. J., Im, J., & Shaw, S. B. (2017). A new optimized algorithm for
887 automating endmember pixel selection in the SEBAL and METRIC models. Remote Sensing of
888 Environment, 196, 178–192. doi:10.1016/j.rse.2017.05.009.

889 Bonan, G. B., Patton, E. G., Finnigan, J. J., Baldocchi, D. D., & Harman, I. N. (2021). Moving beyond
890 the incorrect but useful paradigm: reevaluating big-leaf and multilayer plant canopies to model
891 biosphere-atmosphere fluxes – a review. Agricultural and Forest Meteorology, 306, 108435.
892 https://doi.org/10.1016/j.agrformet.2021.108435

893 Borges, C. K., dos Santos, C. A. C., Carneiro, R. G., da Silva, L. L., de Oliveira, G., Mariano, D., …
894 de S. Medeiros, S. (2020). Seasonal variation of surface radiation and energy balances over two
895 contrasting areas of the seasonally dry tropical forest (Caatinga) in the Brazilian semi-arid.
896 Environmental Monitoring and Assessment, 192(8). doi:10.1007/s10661-020-08484-y

897 Brazil, Ministério do Meio Ambiente. Caatinga. https://antigo.mma.gov.br/biomas/caatinga.html.
898 Acessed: 25 March 2021.

899 Cabral, O. M. R., Freitas, H. C., Cuadra, S. V., de Andrade, C. A., Ramos, N. P., Grutzmacher, P.,
900 … Rossi, P. (2020). The sustainability of a sugarcane plantation in Brazil assessed by the eddy
901 covariance fluxes of greenhouse gases. Agricultural and Forest Meteorology, 282-283, 107864.
902 doi:10.1016/j.agrformet.2019.107864

903 Campos, S., Mendes, K. R., da Silva, L. L., Mutti, P. R., Medeiros, S. S., Amorim, L. B., … Bezerra,
904 B. G. (2019). Closure and partitioning of the energy balance in a preserved area of a Brazilian

905 seasonally dry tropical forest. Agricultural and Forest Meteorology, 271, 398–412.
906 doi:10.1016/j.agrformet.2019.03.018

907 Carvalho, H. F. D. S., de Moura, M. S., da Silva, T. G., & Rodrigues, C. T. (2018). Controlling factors
908 of 'Caatinga' and sugarcane evapotranspiration in the Sub-middle São Francisco Valley. Revista
909 Brasileira de Engenharia Agrícola e Ambiental, 22, 225-230. doi:10.1590/1807-
910 1929/agriambi.v22n4p225-230

911 Chai, T., & Draxler, R. R. (2014). Root mean square error (RMSE) or mean absolute error (MAE)?
912 – Arguments against avoiding RMSE in the literature. Geoscientific Model Development, 7(3), 1247–
913 1250. doi:10.5194/gmd-7-1247-2014

914 Chehbouni, A., Seen, D. L., Njoku, E. G., & Monteny, B. M. (1996). Examination of the difference
915 between radiative and aerodynamic surface temperatures over sparsely vegetated surfaces. Remote
916 Sensing of Environment, 58(2), 177-186. doi: 10.1016/S0034-4257(96)00037-5

917 Chen, J. M., & Liu, J. (2020). Evolution of evapotranspiration models using thermal and shortwave
918 remote sensing data. Remote Sensing of Environment, 237, 111594. doi:10.1016/j.rse.2019.111594

919 Chen, H., Gnanamoorthy, P., Chen, Y., Mansaray, L. R., Song, Q., Liao, K., … Sun, C. (2022).
920 Assessment and Inter-Comparison of Multi-Source High Spatial Resolution Evapotranspiration
921 Products over Lancang–Mekong River Basin, Southeast Asia. Remote Sensing, 14(3), 479.
922 doi:10.3390/rs14030479

923 Cheng, M., Jiao, X., Li, B., Yu, X., Shao, M., & Jin, X. (2021). Long time series of daily
924 evapotranspiration in China based on the SEBAL model and multisource images and validation.
925 Earth System Science Data, 13(8), 3995–4017. doi:10.5194/essd-13-3995-2021

926 Chu, H., et al. (2021) Representativeness of Eddy-Covariance flux footprints for areas surrounding
927 AmeriFlux sites." Agricultural and Forest Meteorology 301-302, 108350.
928 doi:org/10.1016/j.agrformet.2021.108350

929 Costa, J. A.; Navarro-Hevia, J., Costa, C. A. G., & de Araújo, J. C. (2021). Temporal dynamics of
930 evapotranspiration in semiarid native forests in Brazil and Spain using remote sensing. Hydrological
931 Processes, 35(3). doi:10.1002/hyp.14070

932 Costa-Filho, E., Chávez, J. L., Zhang, H., & Andales, A. A. (2021). An optimized surface aerodynamic
933 temperature approach to estimate maize sensible heat flux and evapotranspiration. Agricultural and
934 Forest Meteorology, 311, 108683. doi:10.1016/j.agrformet.2021.108683

935 Cunha, J., Nóbrega, R. L. B., Rufino, I., Erasmi, S., Galvão, C., & Valente, F. (2020). Surface albedo
936 as a proxy for land-cover clearing in seasonally dry forests: Evidence from the Brazilian Caatinga.
937 Remote Sensing of Environment, 238, 111250. doi:10.1016/j.rse.2019.111250

938 Danelichen, V. H. de M., Biudes, M. S., Souza, M. C., Machado, N. G., Silva, B. B. da, & Nogueira,
939 J. de S. (2014). Estimation of soil heat flux in a neotropical Wetland region using remote sensing
940 techniques. Revista Brasileira de Meteorologia, 29(4), 469–482. doi:10.1590/0102-778620120568

941 Dombroski, J. L. D., Praxedes, S. C., de Freitas, R. M. O., & Pontes, F. M. (2011). Water relations
942 of Caatinga trees in the dry season. South African Journal of Botany, 77(2), 430–434.
943 doi:10.1016/j.sajb.2010.11.001

944 Duarte, H. F., Dias, N. L., & Maggiotto, S. R. (2006). Assessing daytime downward longwave
945 radiation estimates for clear and cloudy skies in Southern Brazil. Agricultural and Forest
946 Meteorology, 139(3–4), 171–181. doi:10.1016/j.agrformet.2006.06.008

947 Faivre, R., Colin, J., & Menenti, M. (2017). Evaluation of Methods for Aerodynamic Roughness
948 Length Retrieval from Very High-Resolution Imaging LIDAR Observations over the Heihe Basin in
949 China. Remote Sensing, 9(1), 63. doi:10.3390/rs9010063

950 Farr, T. G., Rosen, P. A., Caro, E., Crippen, R., Duren, R., Hensley, S., ... & Alsdorf, D. (2007). The
951 shuttle radar topography mission. Reviews of geophysics, 45(2). doi:10.1029/2005RG000183

952 Ferreira, T. R., Silva, B. B. D., Moura, M. S. B. D., Verhoef, A., & Nóbrega, R. L. B. (2020). The use
953 of remote sensing for reliable estimation of net radiation and its components: a case study for

954 contrasting land covers in an agricultural hotspot of the Brazilian semiarid region. Agricultural and
955 Forest Meteorology, 291, 108052. doi:10.1016/j.agrformet.2020.108052

956 Foken, T. (2008). The energy balance closure problem: An overview. Ecological Applications, 18(6),
957 1351-1367.doi:10.1890/06-0922.1

958 French, A. N., Hunsaker, D. J., & Thorp, K. R. (2015). Remote sensing of evapotranspiration over
959 cotton using the TSEB and METRIC energy balance models. Remote Sensing of Environment, 158,
960 281–294. doi:10.1016/j.rse.2014.11.003

961 Funk, C., Peterson, P., Landsfeld, M., Pedreros, D., Verdin, J., Shukla, S., ... & Michaelsen, J. (2015).
962 The climate hazards infrared precipitation with stations—a new environmental record for monitoring
963 extremes. Scientific data, 2(1), 1-21. doi:10.1038/sdata.2015.66

964 Gan, R., Zhang, Y., Shi, H., Yang, Y., Eamus, D., Cheng, L., … Yu, Q. (2018). Use of satellite leaf
965 area index estimating evapotranspiration and gross assimilation for Australian ecosystems.
966 Ecohydrology, 11(5), e1974. doi:10.1002/eco.1974

967 Gokmen, M., Vekerdy, Z., Verhoef, A., Verhoef, W., Batelaan, O., & van der Tol, C. (2012).
968 Integration of soil moisture in SEBS for improving evapotranspiration estimation under water stress
969 conditions. Remote Sensing of Environment, 121, 261–274. doi:10.1016/j.rse.2012.02.003

970 Gorelick, N., Hancher, M., Dixon, M., Ilyushchenko, S., Thau, D., & Moore, R. (2017). Google Earth
971 Engine: Planetary-scale geospatial analysis for everyone. Remote Sensing of Environment, 202,
972 18–27. doi:10.1016/j.rse.2017.06.031

973 Gupta, H. V., Sorooshian, S., & Yapo, P. O. (1999). Status of automatic calibration for hydrologic
974 models: Comparison with multilevel expert calibration. Journal of hydrologic engineering, 4(2), 135-
975 143. doi:10.1061/(ASCE)1084-0699(1999)4:2(135)

976 Hallak, R. & Pereira Filho, A. J. (2011). Metodologia para análise de desempenho de simulações de
977 sistemas convectivos na região metropolitana de São Paulo com o modelo ARPS: sensibilidade a

variações com os esquemas de advecção e assimilação de dados. Revista Brasileira de Meteorologia, 26, 591-608.doi:10.1590/S0102-77862011000400009

Hollinger, D. Y., & Richardson, A. D. (2005). Uncertainty in eddy covariance measurements and its application to physiological models. Tree Physiology, 25(7), 873–885. doi:10.1093/treephys/25.7.873

Jaafar, H., Mourad, R., & Schull, M. (2022). A global 30-m ET model (HSEB) using harmonized Landsat and Sentinel-2, MODIS and VIIRS: Comparison to ECOSTRESS ET and LST. Remote Sensing of Environment, 274, 112995. doi:10.1016/j.rse.2022.112995

Jia, L., Su, Z., van den Hurk, B., Menenti, M., Moene, A., De Bruin, H. A. ., … Cuesta, A. (2003). Estimation of sensible heat flux using the Surface Energy Balance System (SEBS) and ATSR measurements. Physics and Chemistry of the Earth, Parts A/B/C, 28(1-3), 75–88. doi:10.1016/s1474-7065(03)00009-3

Kayser, R. H., Ruhoff, A., Laipelt, L., de Mello Kich, E., Roberti, D. R., de Arruda Souza, V., ... & Neale, C. M. U. (2022). Assessing geeSEBAL automated calibration and meteorological reanalysis uncertainties to estimate evapotranspiration in subtropical humid climates. Agricultural and Forest Meteorology, 314, 108775. doi:10.1016/j.agrformet.2021.108775

Koch, R., Almeida-Cortez, J. S., & Kleinschmit, B. (2017). Revealing areas of high nature conservation importance in a seasonally dry tropical forest in Brazil: Combination of modelled plant diversity hot spots and threat patterns. Journal for Nature Conservation, 35, 24–39. doi:10.1016/j.jnc.2016.11.004

Kustas, W., Choudhury, B. Moran, M., Reginato, R., Jackson, R., Gay, L., & Weaver, H. (1989a). Determination of sensible heat flux over sparse canopy using thermal infrared data. Agricultural and Forest Meteorology, 44(3-4), 197–216. doi:10.1016/0168-1923(89)90017-8

1001 Kustas, W. P., Choudhury, B. J., Kunkel, K. E., & Gay, L. W. (1989b). Estimate of the aerodynamic
1002 roughness parameters over an incomplete canopy cover of cotton. Agricultural and Forest
1003 Meteorology, 46(1-2), 91-105. doi:10.1016/0168-1923(89)90114-7

1004 Laipelt, L., Ruhoff, A. L., Fleischmann, A. S., Kayser, R. H. B., Kich, E. de M., da Rocha, H. R., &
1005 Neale, C. M. U. (2020). Assessment of an Automated Calibration of the SEBAL Algorithm to Estimate
1006 Dry-Season Surface-Energy Partitioning in a Forest–Savanna Transition in Brazil. Remote Sensing,
1007 12(7), 1108. doi:10.3390/rs12071108

1008 Laipelt, L., Henrique Bloedow Kayser, R., Santos Fleischmann, A., Ruhoff, A., Bastiaanssen, W.,
1009 Erickson, T. A., & Melton, F. (2021). Long-term monitoring of evapotranspiration using the SEBAL
1010 algorithm and Google Earth Engine cloud computing. ISPRS Journal of Photogrammetry and
1011 Remote Sensing, 178, 81–96. doi:10.1016/j.isprsjprs.2021.05.018

1012 Lhomme, J. P., Chehbouni, A., & Monteny, B. (2000). Sensible Heat Flux-Radiometric Surface
1013 Temperature Relationship Over Sparse Vegetation: Parameterizing B-1. Boundary-Layer
1014 Meteorology, 97(3), 431–457. doi:10.1023/a:1002786402695

1015 Liao, J. J., & Lewis, J. W. (2000). A note on concordance correlation coefficient. PDA Journal of
1016 Pharmaceutical Science and Technology, 54(1), 23-26.

1017 Lima, A. L. A., & Rodal, M. J. N. (2010). Phenology and wood density of plants growing in the semi-
1018 arid region of northeastern Brazil. Journal of Arid Environments, 74(11), 1363–1373.
1019 doi:10.1016/j.jaridenv.2010.05.009

1020 Lima, A. L. A., Sá Barretto Sampaio, E. V., Castro, C. C., Rodal, M. J. N., Antonino, A. C. D., & de
1021 Melo, A. L. (2012). Do the phenology and functional stem attributes of woody species allow for the
1022 identification of functional groups in the semiarid region of Brazil? Trees, 26(5), 1605–1616.
1023 doi:10.1007/s00468-012-0735-2

1024 Lima, C. E. S. de, Costa, V. S. de O., Galvíncio, J. D., Silva, R. M. da, & Santos, C. A. G. (2021).
1025 Assessment of automated evapotranspiration estimates obtained using the GP-SEBAL algorithm for

1026 dry forest vegetation (Caatinga) and agricultural areas in the Brazilian semiarid region. Agricultural
1027 Water Management, 250, 106863. doi:10.1016/j.agwat.2021.106863

1028 Lin, L. K. (1989). A concordance correlation coefficient to evaluate reproducibility. Biometrics, 45(1),
1029 255–268. https://doi.org/10.2307/2532051

1030 Liu, S., Lu, L., Mao, D., & Jia, L. (2007). Evaluating parameterizations of aerodynamic resistance to
1031 heat transfer using field measurements. Hydrology and Earth System Sciences, 11(2), 769–783.
1032 doi:10.5194/hess-11-769-2007

1033 Liu, Y., Guo, W., Huang, H., Ge, J., & Qiu, B. (2021). Estimating global aerodynamic parameters in
1034 1982–2017 using remote-sensing data and a turbulent transfer model. Remote Sensing of
1035 Environment, 260, 112428. doi:10.1016/j.rse.2021.112428

1036 Long, D., Gao, Y., & Singh, V. P. (2010). Estimation of daily average net radiation from MODIS data
1037 and DEM over the Baiyangdian watershed in North China for clear sky days. Journal of Hydrology,
1038 388(3–4), 217–233. doi:10.1016/j.jhydrol.2010.04.042

1039 Long, D., Singh, V. P., & Li, Z.-L. (2011). How sensitive is SEBAL to changes in input variables,
1040 domain size and satellite sensor? Journal of Geophysical Research: Atmospheres, 116(D21).
1041 Portico. doi:10.1029/2011jd016542

1042 Maia, V. A., de Souza, C. R., de Aguiar-Campos, N., Fagundes, N. C. A., Santos, A. B. M., de Paula,
1043 G. G. P., … dos Santos, R. M. (2020). Interactions between climate and soil shape tree community
1044 assembly and above-ground woody biomass of tropical dry forests. Forest Ecology and
1045 Management, 474, 118348. doi:10.1016/j.foreco.2020.118348

1046 Mallick, K., Wandera, L., Bhattarai, N., Hostache, R., Kleniewska, M., & Chormanski, J. (2018). A
1047 critical evaluation on the role of aerodynamic and canopy–surface conductance parameterization in
1048 SEB and SVAT models for simulating evapotranspiration: A case study in the Upper Biebrza National
1049 Park Wetland in Poland. Water, 10(12), 1753. doi.org/10.3390/w10121753

1050 Marques, T. V., Mendes, K., Mutti, P., Medeiros, S., Silva, L., Perez-Marin, A. M., … Bezerra, B.
1051 (2020). Environmental and biophysical controls of evapotranspiration from Seasonally Dry Tropical
1052 Forests (Caatinga) in the Brazilian Semiarid. Agricultural and Forest Meteorology, 287, 107957.
1053 doi:10.1016/j.agrformet.2020.107957

1054 McShane, R. R., Driscoll, K. P., & Sando, R. (2017). A review of surface energy balance models for
1055 estimating actual evapotranspiration with remote sensing at high spatiotemporal resolution over
1056 large extents. Scientific Investigations Report. doi:10.3133/sir20175087

1057 Medeiros, R., Andrade, J., Ramos, D., Moura, M., Pérez-Marin, A., dos Santos, C., … Cunha, J.
1058 (2022). Remote Sensing Phenology of the Brazilian Caatinga and Its Environmental Drivers. Remote
1059 Sensing, 14(11), 2637. doi:10.3390/rs14112637

1060 Meier, R., Davin, E. L., Swenson, S. C., Lawrence, D. M., & Schwaab, J. (2019). Biomass heat
1061 storage dampens diurnal temperature variations in forests. Environmental Research Letters, 14(8),
1062 084026. doi:10.1088/1748-9326/ab2b4e

1063 Melo, D. C. D., Anache, J. A. A., Borges, V. P., Miralles, D. G., Martens, B., Fisher, J. B., …
1064 Wendland, E. (2021). Are remote sensing evapotranspiration models reliable across South American
1065 ecoregions? Water Resources Research, 57(11). doi:10.1029/2020wr028752

1066 Mhawej, M., Caiserman, A., Nasrallah, A., Dawi, A., Bachour, R., & Faour, G. (2020). Automated
1067 evapotranspiration retrieval model with missing soil-related datasets: The proposal of SEBALI.
1068 Agricultural Water Management, 229, 105938. doi:10.1016/j.agwat.2019.105938

1069 Miles, L., Newton, A. C., DeFries, R. S., Ravilious, C., May, I., Blyth, S., … Gordon, J. E. (2006). A
1070 global overview of the conservation status of tropical dry forests. Journal of Biogeography, 33(3),
1071 491–505. doi:10.1111/j.1365-2699.2005.01424.x

1072 Miranda, R. Q., Nóbrega, R. L. B., Moura, M. S. B., Raghavan, S., & Galvíncio, J. D. (2020). Realistic
1073 and simplified models of plant and leaf area indices for a seasonally dry tropical forest. International

1074 Journal of Applied Earth Observation and Geoinformation, 85, 101992.
1075 doi:10.1016/j.jag.2019.101992

1076 Miranda, R. D. Q., Galvincio, J. D., Morais, Y. C. B., Moura, M. S. B. D., Jones, C. A., & Srinivasan,
1077 R. (2018). Dry forest deforestation dynamics in Brazil's Pontal Basin. Revista Caatinga, 31, 385-395.
1078 doi:10.1590/1983-21252018v31n215rc

1079 Mohan, M. M. P., Kanchirapuzha, R., & Varma, M. R. R. (2020a). Review of approaches for the
1080 estimation of sensible heat flux in remote sensing-based evapotranspiration models. Journal of
1081 Applied Remote Sensing, 14(04). doi:10.1117/1.jrs.14.041501

1082 Mohan, M. P.; Kanchirapuzha, R., & Varma, M. R. R. (2020b). Integration of soil moisture as an
1083 auxiliary parameter for the anchor pixel selection process in SEBAL using Landsat 8 and Sentinel-
1084 1A images. International Journal of Remote Sensing, 41(3), 1214-1231.

1085 Moro, M. F., Silva, I. A., Araújo, F. S. de, Nic Lughadha, E., Meagher, T. R., & Martins, F. R. (2015).
1086 The role of edaphic environment and climate in structuring phylogenetic pattern in Seasonally Dry
1087 Tropical Plant Communities. PLOS ONE, 10(3), e0119166. doi:10.1371/journal.pone.0119166

1088 Moro, M. F., Nic Lughadha, E., de Araújo, F. S., & Martins, F. R. (2016). A Phytogeographical
1089 Metaanalysis of the Semiarid Caatinga domain in Brazil. The Botanical Review, 82(2), 91–148.
1090 doi:10.1007/s12229-016-9164-z

1091 Mu, Q., Zhao, M., & Running, S. W. (2011). Improvements to a MODIS global terrestrial
1092 evapotranspiration algorithm. Remote Sensing of Environment, 115(8), 1781–1800.
1093 doi:10.1016/j.rse.2011.02.019

1094 Muñoz Sabater, J., (2019): ERA5-Land hourly data from 1981 to present. Copernicus Climate
1095 Change Service (C3S) Climate Data Store (CDS). (Accessed on 23-Feb-2022),
1096 doi:10.24381/cds.e2161bac

1097 Mutti, P. R., da Silva, L. L., Medeiros, S. de S., Dubreuil, V., Mendes, K. R., Marques, T. V., …
1098 Bezerra, B. G. (2019). Basin scale rainfall-evapotranspiration dynamics in a tropical semiarid

environment during dry and wet years. International Journal of Applied Earth Observation and Geoinformation, 75, 29–43. doi:10.1016/j.jag.2018.10.007

Murray, T., and Verhoef, A. (2007) Moving towards a more mechanistic approach in the determination of soil heat flux from remote measurements. II. Diurnal shape of soil heat flux. Agricultural and Forest Meteorology, 147: 88-97.

Nash, J. E., & Sutcliffe, J. V. (1970). River flow forecasting through conceptual models part I - A discussion of principles. Journal of Hydrology, 10(3), 282–290. doi:10.1016/0022-1694(70)90255-6

Oliveira, M. L., Santos, C. A. C., Oliveira, G., Perez-Marin, A. M., & Santos, C. A. G. (2021). Effects of human-induced land degradation on water and carbon fluxes in two different Brazilian dryland soil covers. Science of the Total Environment, 792, 148458. doi:10.1016/j.scitotenv.2021.148458

Owen, P. R., & Thomson, W. R. (1963). Heat transfer across rough surfaces. Journal of Fluid Mechanics, 15(3), 321–334. doi:10.1017/s0022112063000288

Paloschi, R. A., Ramos, D. M., Ventura, D. J., Souza, R., Souza, E., Morellato, L. P. C., … Borma, L. D. S. (2020). Environmental drivers of water use for Caatinga woody plant species: Combining remote sensing phenology and sap flow measurements. Remote Sensing, 13(1), 75. doi:10.3390/rs13010075

Paul, G., Gowda, P. H., Vara Prasad, P. V., Howell, T. A., Staggenborg, S. A., & Neale, C. M. U. (2013). Lysimetric evaluation of SEBAL using high resolution airborne imagery from BEAREX08. Advances in Water Resources, 59, 157–168. doi:10.1016/j.advwatres.2013.06.003

Paul, G., Gowda, P. H., Vara Prasad, P. V., Howell, T. A., Aiken, R. M., & Neale, C. M. U. (2014). Investigating the influence of roughness length for heat transport (zoh) on the performance of SEBAL in semi-arid irrigated and dryland agricultural systems. Journal of Hydrology, 509, 231–244. doi:10.1016/j.jhydrol.2013.11.040

1122 Paulson, C. A. (1970). The mathematical representation of wind speed and temperature profiles in
1123 the unstable atmospheric surface layer. Journal of Applied Meteorology and Climatology, 9(6), 857-
1124 861. doi:10.1175/1520-0450(1970)009%3C0857:tmrows%3E2.0.co;2

1125 Pennington, R. T., Lewis, G. P., & Ratter, J. A. (Eds.). (2006). An overview of the plant diversity,
1126 biogeography and conservation of Neotropical Savannas and Seasonally Dry Forests. Neotropical
1127 Savannas and Seasonally Dry Forests, 1–29. doi:10.1201/9781420004496-1

1128 Pennington, R. T., Lavin, M., & Oliveira-Filho, A. (2009). Woody plant diversity, evolution, and
1129 ecology in the Tropics: Perspectives from Seasonally Dry Tropical Forests. Annual Review of
1130 Ecology, Evolution, and Systematics, 40(1), 437–457. doi:10.1146/annurev.ecolsys.110308.120327

1131 Pennington, R. T., Lehmann, C. E. R., & Rowland, L. M. (2018). Tropical savannas and dry forests.
1132 Current Biology, 28(9), R541–R545. doi:10.1016/j.cub.2018.03.014

1133 Potapov, P., Li, X., Hernandez-Serna, A., Tyukavina, A., Hansen, M. C., Kommareddy, A., … Hofton,
1134 M. (2021). Mapping global forest canopy height through integration of GEDI and Landsat data.
1135 Remote Sensing of Environment, 253, 112165. doi:10.1016/j.rse.2020.112165

1136 Priestley, C. H. B., & Taylor, R. J. (1972). On the assessment of surface heat flux and evaporation
1137 using large-scale parameters. Monthly Weather Review, 100(2), 81–92. doi:10.1175/1520-
1138 0493(1972)100<0081:otaosh>2.3.co;2

1139 Queiroz, L. P., Cardoso, D., Fernandes, M. F., & Moro, M. F. (2017). Diversity and evolution of
1140 flowering plants of the Caatinga domain. Caatinga, 23–63. doi:10.1007/978-3-319-68339-3_2

1141 Queiroz, M. G. D., Silva, T. G. F. D., Souza, C. A. A. D., Jardim, A. M. D. R. F., Araújo Júnior, G. D.
1142 N., Souza, L. S. B. D., & Moura, M. S. B. D. (2020). Composition of Caatinga species under anthropic
1143 disturbance and its correlation with rainfall partitioning. Floresta e Ambiente, 28. doi:10.1590/2179-
1144 8087-FLORAM-2019-0044

1145 Ramoelo, A., Majozi, N., Mathieu, R., Jovanovic, N., Nickless, A., & Dzikiti, S. (2014). Validation of
1146 global evapotranspiration product (MOD16) using flux tower data in the African Savanna, South
1147 Africa. Remote Sensing, 6(8), 7406–7423. doi:10.3390/rs6087406

1148 Rasp, S., Pritchard, M. S., & Gentine, P. (2018). Deep learning to represent subgrid processes in
1149 climate models. Proceedings of the National Academy of Sciences, 115(39), 9684–9689.
1150 doi:10.1073/pnas.1810286115

1151 Raupach, M. R. (1992). Drag and drag partition on rough surfaces. Boundary-Layer Meteorology,
1152 60(4), 375–395. doi.org/10.1007/bf00155203

1153 Raupach, M. R. (1994). Simplified expressions for vegetation roughness length and zero-plane
1154 displacement as functions of canopy height and area index. Boundary-Layer Meteorology, 71(1–2),
1155 211–216. doi:10.1007/bf00709229

1156 Roberts, W., Williams, G. P., Jackson, E., Nelson, E. J., & Ames, D. P. (2018). Hydrostats: A Python
1157 package for characterizing errors between observed and predicted time series. Hydrology, 5(4), 66.
1158 doi:10.3390/hydrology5040066

1159 Rodell, M., Houser, P. R., Jambor, U., Gottschalck, J., Mitchell, K., Meng, C.-J., … Toll, D. (2004).
1160 The Global Land Data Assimilation System. Bulletin of the American Meteorological Society, 85(3),
1161 381–394. doi:10.1175/bams-85-3-381

1162 Running, S., Mu, Q., Zhao, M. (2017). MOD16A2 MODIS/Terra Net Evapotranspiration 8-Day L4
1163 Global 500m SIN Grid V006 [Data set]. NASA EOSDIS Land Processes DAAC. Accessed 23-Feb-
1164 2022 from doi:10.5067/MODIS/MOD16A2.006

1165 Sahnoun, F., Abderrahmane, H., Kaddour, M., Abdelkader, K., Mohamed, B., & Castro, T. A. H. D.
1166 (2021). Application of SEBAL and T s/VI trapezoid models for estimating actual evapotranspiration
1167 in the Algerian Semi-Arid Environment to improve agricultural water management. Revista Brasileira
1168 de Meteorologia, 36, 219-236. doi:10.1590/0102-77863610020

1169 Salazar-Martínez, D., Holwerda, F., Holmes, T. R. H., Yépez, E. A., Hain, C. R., Alvarado-Barrientos,
1170 S., … Vivoni, E. R. (2022). Evaluation of remote sensing-based evapotranspiration products at low-
1171 latitude eddy covariance sites. Journal of Hydrology, 610, 127786.
1172 doi:10.1016/j.jhydrol.2022.127786

1173 Santos, R. M., Oliveira-Filho, A. T., Eisenlohr, P. V., Queiroz, L. P., Cardoso, D. B. O. S., & Rodal,
1174 M. J. N. (2012). Identity and relationships of the Arboreal Caatinga among other floristic units of
1175 seasonally dry tropical forests (SDTFs) of north-eastern and Central Brazil. Ecology and Evolution,
1176 2(2), 409–428. doi:10.1002/ece3.91

1177 Santos, M. G., Oliveira, M. T., Figueiredo, K. V., Falcão, H. M., Arruda, E. C. P., Almeida-Cortez, J.,
1178 … Antonino, A. C. D. (2014). Caatinga, the Brazilian dry tropical forest: can it tolerate climate
1179 changes? Theoretical and Experimental Plant Physiology, 26(1), 83–99. doi:10.1007/s40626-014-
1180 0008-0

1181 Santos, C. A. C., Mariano, D. A., das Chagas A. do Nascimento, F., da C. Dantas, F. R., de Oliveira,
1182 G., Silva, M. T., … Neale, C. M. U. (2020). Spatio-temporal patterns of energy exchange and
1183 evapotranspiration during an intense drought for drylands in Brazil. International Journal of Applied
1184 Earth Observation and Geoinformation, 85, 101982. doi:10.1016/j.jag.2019.101982

1185 Schaaf, C., & Wang, Z. (2015). MCD43A4 MODIS/Terra+Aqua BRDF/Albedo Nadir BRDF Adjusted
1186 Ref Daily L3 Global - 500m V006 [Data set]. NASA EOSDIS Land Processes DAAC. Accessed 23-
1187 Feb-2022. doi:10.5067/MODIS/MCD43A4.006

1188 Senay, G. B., Bohms, S., Singh, R. K., Gowda, P. H., Velpuri, N. M., Alemu, H., & Verdin, J. P.
1189 (2013). Operational evapotranspiration mapping using remote sensing and weather datasets: A new
1190 parameterization for the SSEB approach. JAWRA Journal of the American Water Resources
1191 Association, 49(3), 577–591. Portico. https://doi.org/10.1111/jawr.12057

1192 Senay, G. B., Friedrichs, M., Morton, C., Parrish, G. E., Schauer, M., Khand, K., ... & Huntington, J.
1193 (2022). Mapping actual evapotranspiration using Landsat for the conterminous United States:

1194 Google Earth Engine implementation and assessment of the SSEBop model. Remote Sensing of
1195 Environment, 275, 113011. doi:10.1016/j.rse.2022.113011

1196 Senkondo, W., Munishi, S. E., Tumbo, M., Nobert, J., & Lyon, S. W. (2019). Comparing remotely-
1197 sensed surface energy balance evapotranspiration estimates in heterogeneous and data-limited
1198 regions: a case study of Tanzania's Kilombero Valley. Remote Sensing, 11(11), 1289.
1199 doi:10.3390/rs11111289

1200 Shuttleworth, W. J. (2012). Terrestrial hydrometeorology. John Wiley & Sons.

1201 Silva, A. M., da Silva, R. M., & Santos, C. A. G. (2019). Automated surface energy balance algorithm
1202 for land (ASEBAL) based on automating endmember pixel selection for evapotranspiration
1203 calculation in MODIS orbital images. International Journal of Applied Earth Observation and
1204 Geoinformation, 79, 1–11. doi:10.1016/j.jag.2019.02.012

1205 Silva, J. M. C.; LEAL, I.R.; Tabarelli, M. (Ed.). (2017a). Caatinga: the largest tropical dry forest region
1206 in South America. Springer.

1207 Silva, P. F. da, Lima, J. R. de S., Antonino, A. C. D., Souza, R., Souza, E. S. de, Silva, J. R. I., &
1208 Alves, E. M. (2017b). Seasonal patterns of carbon dioxide, water and energy fluxes over the
1209 Caatinga and grassland in the semi-arid region of Brazil. Journal of Arid Environments, 147, 71–82.
1210 doi:10.1016/j.jaridenv.2017.09.003

1211 Singh, R. K., & Irmak, A. (2011). Treatment of anchor pixels in the METRIC model for improved
1212 estimation of sensible and latent heat fluxes. Hydrological Sciences Journal, 56(5), 895–906.
1213 doi:10.1080/02626667.2011.587424

1214 Singh, R. K., Liu, S., Tieszen, L. L., Suyker, A. E., & Verma, S. B. (2012). Estimating seasonal
1215 evapotranspiration from temporal satellite images. Irrigation Science, 30(4), 303-313.
1216 doi:10.1007/s00271-011-0287-z

1217 Souza, L. S. B. de, Moura, M. S. B. de, Sediyama, G. C., & Silva, T. G. F. da. (2015). Balanço de
1218 energia e controle biofísico da evapotranspiração na Caatinga em condições de seca intensa.
1219 Pesquisa Agropecuária Brasileira, 50(8), 627–636. doi:10.1590/s0100-204x2015000800001

1220 Stewart, J. B., Kustas, W. P., Humes, K. S., Nichols, W. D., Moran, M. S., & de Bruin, H. A. (1994).
1221 Sensible heat flux-radiometric surface temperature relationship for eight semiarid areas. Journal of
1222 Applied Meteorology and Climatology, 33(9), 1110-1117. doi:10.1175/1520-
1223 0450(1994)033%3C1110:shfrst%3E2.0.co;2

1224 Su, Z., Schmugge, T., Kustas, W. P., & Massman, W. J. (2001). An evaluation of two models for
1225 estimation of the roughness height for heat transfer between the land surface and the atmosphere.
1226 Journal of Applied Meteorology, 40(11), 1933-1951. doi:10.1175/1520-
1227 0450(2001)040%3C1933:aeotmf%3E2.0.co;2

1228 Su, Z. (2002). The Surface Energy Balance System (SEBS) for estimation of turbulent heat fluxes.
1229 Hydrology and Earth System Sciences, 6(1), 85–100. doi:10.5194/hess-6-85-2002

1230 Swenson, S. C., Burns, S. P., & Lawrence, D. M. (2019). The Impact of Biomass Heat Storage on
1231 the Canopy Energy Balance and Atmospheric Stability in the Community Land Model. Journal of
1232 Advances in Modeling Earth Systems, 11(1), 83–98. Portico. doi:10.1029/2018ms001476

1233 Teixeira, A. D. C., Bastiaanssen, W. G., Ahmad, M., & Bos, M. G. (2009). Reviewing SEBAL input
1234 parameters for assessing evapotranspiration and water productivity for the Low-Middle Sao
1235 Francisco River basin, Brazil: Part A: Calibration and validation. Agricultural and Forest Meteorology,
1236 149(3-4), 462-476. doi:10.1016/j.agrformet.2008.09.016

1237 Thom, A. S. (1972). Momentum, mass and heat exchange of vegetation. Quarterly Journal of the
1238 Royal Meteorological Society, 98(415), 124–134. doi:10.1002/qj.49709841510

1239 Tomasella, J., Silva Pinto Vieira, R. M., Barbosa, A. A., Rodriguez, D. A., Oliveira Santana, M. de, &
1240 Sestini, M. F. (2018). Desertification trends in the Northeast of Brazil over the period 2000–2016.

International Journal of Applied Earth Observation and Geoinformation, 73, 197–206. doi:10.1016/j.jag.2018.06.012

Trebs, I., Mallick, K., Bhattarai, N., Sulis, M., Cleverly, J., Woodgate, W., Silberstein, R., Hinko-Najera, N., Beringer, J., Meyer, W. S., Su, Z., & Boulet, G. (2021). The role of aerodynamic resistance in thermal remote sensing-based evapotranspiration models. EGU General Assembly. doi.org/10.5194/egusphere-egu21-2186Remote Sensing of Environment, 264, 112602. doi:10.1016/j.rse.2021.112602

Trezza, R. (2006). Evapotranspiration from a remote sensing model for water management in an irrigation system in Venezuela. Interciencia, 31(6), 417-423

Trezza, R., Allen, R., & Tasumi, M. (2013). Estimation of Actual Evapotranspiration along the Middle Rio Grande of New Mexico Using MODIS and Landsat Imagery with the METRIC Model. Remote Sensing, 5(10), 5397–5423. doi:10.3390/rs5105397

Troufleau, D., Lhomme, J. P., Monteny, B., & Vidal, A. (1997). Sensible heat flux and radiometric surface temperature over sparse Sahelian vegetation. I. An experimental analysis of the kB−1 parameter. Journal of Hydrology, 188, 815-838. doi:10.1016/s0022-1694(96)03172-1

Verhoef, A., De Bruin, H. A. R., & Van Den Hurk, B. J. J. M. (1997a). Some practical notes on the parameter kB−1 for sparse vegetation. Journal of Applied Meteorology, 36(5), 560-572. doi:10.1175/1520-0450(1997)036%3C0560:spnotp%3E2.0.co;2

Verhoef, A., McNaughton, K. G., & Jacobs, A. F. G. (1997b). A parameterization of momentum roughness length and displacement height for a wide range of canopy densities. Hydrology and Earth System Sciences, 1(1), 81–91. doi:10.5194/hess-1-81-1997

Wang, C., Yang, J., Myint, S. W., Wang, Z.-H., & Tong, B. (2016). Empirical modeling and spatio-temporal patterns of urban evapotranspiration for the Phoenix metropolitan area, Arizona. GIScience & Remote Sensing, 53(6), 778–792. doi:10.1080/15481603.2016.1243399

Wilson, K., Goldstein, A., Falge, E., Aubinet, M., Baldocchi, D., Berbigier, P., … Verma, S. (2002). Energy balance closure at FLUXNET sites. Agricultural and Forest Meteorology, 113(1-4), 223–243. doi:10.1016/s0168-1923(02)00109-0

WRB, I.W.G., 2006. World reference base for soil resources 2006, 2nd ed. In: FAO (ed.), World Soil Resources Reports No. 103, Rome. ISBN 92-5-105511-4.

Wu, Q. (2020). geemap: A Python package for interactive mapping with Google Earth Engine. Journal of Open Source Software, 5(51), 2305. doi:10.21105/joss.02305

Yin, L., Wang, X., Feng, X., Fu, B., & Chen, Y. (2020). A comparison of SSEBop-Model-Based evapotranspiration with eight evapotranspiration products in the Yellow River Basin, China. Remote Sensing, 12(16), 2528. doi:10.3390/rs12162528

Zhang, Y., Kong, D., Gan, R., Chiew, F. H. S., McVicar, T. R., Zhang, Q., & Yang, Y. (2019). Coupled estimation of 500 m and 8-day resolution global evapotranspiration and gross primary production in 2002–2017. Remote Sensing of Environment, 222, 165–182. doi:10.1016/j.rse.2018.12.031

Zhao, M., Heinsch, F. A., Nemani, R. R., & Running, S. W. (2005). Improvements of the MODIS terrestrial gross and net primary production global data set. Remote sensing of Environment, 95(2), 164-176. doi:10.1016/j.rse.2004.12.011